

Bubble formation in active binary mixture model

Kyosuke Adachi^{1,2}

¹*RIKEN Center for Interdisciplinary Theoretical and Mathematical Sciences, 2-1 Hirosawa, Wako 351-0198, Japan*

²*Nonequilibrium Physics of Living Matter Laboratory,*

RIKEN Pioneering Research Institute, 2-1 Hirosawa, Wako 351-0198, Japan

(Dated: June 5, 2025)

Phase separation, the spontaneous segregation of density, is a ubiquitous phenomenon observed across diverse physical and biological systems. Within a crowd of self-propelled elements, active phase separation emerges from the interplay of activity and density interactions. A striking feature of active phase separation is the persistent formation of dilute-phase bubbles within the dense phase, which has been explored in theoretical models. However, the fundamental parameters that systematically control bubble formation remain unclear in conventional active particle models. Here, we introduce an active binary mixture model, where active solutes and solvents dynamically exchange their positions, and find that spontaneous bubble formation can be tuned by the asymmetry in their activities. Numerical simulations reveal that moderate solvent activity enhances bubble formation, while larger solvent activity, comparable to solute activity, suppresses it. By employing mean-field theory, which captures essential phase behaviors, we consider the mechanism for the enhancement of bubble formation induced by solvent activity. Beyond these findings, when solute and solvent activities are equal, numerical simulations indicate that critical phenomena of active phase separation under the suppression of bubbles belong to the Ising universality class. Our findings establish activity asymmetry as a key control parameter for active matter phase transitions, offering new insights into universality in nonequilibrium systems.

I. INTRODUCTION

Active matter exhibits diverse collective phenomena, ranging from giant number fluctuations [1, 2] to active turbulence [3], depending on the type of activity of constituents and their interactions [4–6]. Experimentally, collective properties of active matter have been investigated extensively using biological matter [7–11] and artificial systems [12–21]. From theoretical viewpoints, the effects of activity have been studied using particle models such as the Vicsek model [22] and coarse-grained models such as the Toner-Tu model [23]. Activity has been shown to produce material phases that are distinct from equilibrium counterparts [24, 25]; for example, flocking transitions can spontaneously break continuous symmetry even in two dimensions [23, 26–29] or lead to metastable ordering [30–32].

Active phase separation [33], also called motility-induced phase separation [34], is a prototypical example of collective phenomena in active matter, where activity and density-dependent interactions induce the self-aggregation of particles. Detailed properties of active phase separation have been investigated using particle models such as active Brownian particles [35], active Ornstein-Uhlenbeck particles [36], and active lattice gas [37], as well as coarse-grained models called Active Model B (AMB) [38] and Active Model B+ (AMB+) [39]. Since the microscopic mechanism for active phase separation is distinct from that for equilibrium phase separation, special features of the former, such as spontaneous velocity alignment [40], have been found in numerical studies. However, the emergence of their similarities in macroscale behaviors has also been discussed [34, 41]; for example, effective free energy has been constructed for AMB [42, 43].

Compared to equilibrium phase separation, persistent formation of dilute-phase bubbles within the dense phase is a unique feature of active phase separation [39, 44–49]. A mean-field analysis of AMB+ has suggested that the λ and

ζ terms, which break time-reversal symmetry and the symmetry between the dense and dilute phases, are crucial for bubble formation [39]. Bubbles qualitatively change the phase behavior in large systems, leading to bubbly phase separation [39, 49] or microphase separation [39, 46] instead of macroscopic phase separation, which is typically observed in equilibrium [50]. Despite the significance of bubbles in active phase separation, it is still unclear what parameters can systematically control bubble formation in active particle models, except for a few numerical examples [47]. In addition, large-scale and long-time simulations are required to investigate the properties of bubbles in typical particle models [46].

Bubbles have also been suspected to affect the critical behavior of active phase separation [33, 44, 46, 51], which may [52–55] or may not [56, 57] belong to the Ising universality class, i.e., the universality class for equilibrium phase separation [58]. To address this question using active particle models, investigation of critical phenomena under the suppression of bubbles would provide a useful baseline; in the regime with negligible effects of bubbles, the Ising universality is expected to appear, according to renormalization group analyses of coarse-grained models [44, 52]. More generally, by highlighting critical phenomena, active matter systems can be systematically connected to nonequilibrium models in other disciplines, such as socioeconomic systems [59].

In this study, we propose an active binary mixture model, where active solutes and solvents stochastically exchange their positions. By conducting numerical simulations, we find that bubble formation in active phase separation is controlled by the asymmetry in activity between solutes and solvents. Without solvent activity, this model is equivalent to active lattice gas and undergoes phase separation by solute activity, where bubbles of solvents can gradually appear as the system size increases. In contrast, with moderate solvent activity, we observe enhanced bubble formation even in relatively small systems, leading to a power-law distribution of the bubble

size. Mean-field theory qualitatively reproduces the nonstationary state with persistent bubble formation, even though the mean-field dynamics is deterministic. Larger solvent activity that is comparable to solute activity, in turn, suppresses bubbles due to the symmetry between solutes and solvents. Near the phase-separation transition line, we find that solute and solvent activities compete with each other, which is explained by linear stability analysis of mean-field theory. Lastly, when solute and solvent activities are equal, numerical simulations suggest that critical phenomena of active phase separation under the suppression of bubbles belong to the Ising universality class.

II. ACTIVE BINARY MIXTURE MODEL

Motivated by lattice solution models for equilibrium phase separation (e.g., the Flory-Huggins model [50]), we consider an active binary mixture model (Fig. 1). Each site of a rectangular lattice with size (L_x, L_y) is occupied by a solute or solvent with polarity $p \in \{\rightarrow, \uparrow, \leftarrow, \downarrow\}$, which represents the direction of activity. We assume two kinds of stochastic dynamics: (i) onsite rotation of polarity by $+90^\circ$ or -90° , each at rate γ , and (ii) exchange of neighboring solute and solvent at a rate depending on the configuration; the passive exchange rate is 1 independent of polarity or moving direction, and the additional active exchange rate is ϵ_{solute} ($\epsilon_{\text{solvent}}$) for the exchange that corresponds to the motion of solute (solvent) in the polarity direction [see examples in Fig. 1(ii)]. We take the lattice constant as unity, assume periodic boundary conditions along the x and y axes, and write the mean density (i.e., occupancy) of solutes as $\rho \in (0, 1)$. For the numerical simulations in the following, we fix the rotation rate as $\gamma = 0.1$ and examine the change in collective behaviors when we change the solute activity ϵ_{solute} , solvent activity $\epsilon_{\text{solvent}}$, and solute density ρ (see Appendix A 1 for the implementation of stochastic dynamics).

Without solvent activity ($\epsilon_{\text{solvent}} = 0$), this model is equivalent to the active lattice gas [37, 52, 60–62], where solutes with large solute activity ϵ_{solute} undergo self-aggregation, i.e., active phase separation. By introducing $\epsilon_{\text{solvent}} > 0$, we expect that solvents will also tend to aggregate due to their activity, which might help phase separation cooperatively with solute activity; however, the effect of solvent activity is not so simple, as we discuss below. For the symmetric limit ($\epsilon_{\text{solute}} = \epsilon_{\text{solvent}}$), the solutes and solvents behave equivalently, and thus the critical density for phase separation should be located at $\rho = 0.5$ from symmetry.

In the following, we mainly focus on the case with $\epsilon_{\text{solute}} \geq \epsilon_{\text{solvent}}$ and investigate the phase behavior by numerical simulations (Sec. III) and mean-field theory (Sec. IV). Then we consider the symmetric limit ($\epsilon_{\text{solute}} = \epsilon_{\text{solvent}}$) and examine the critical properties for active phase separation (Sec. V).

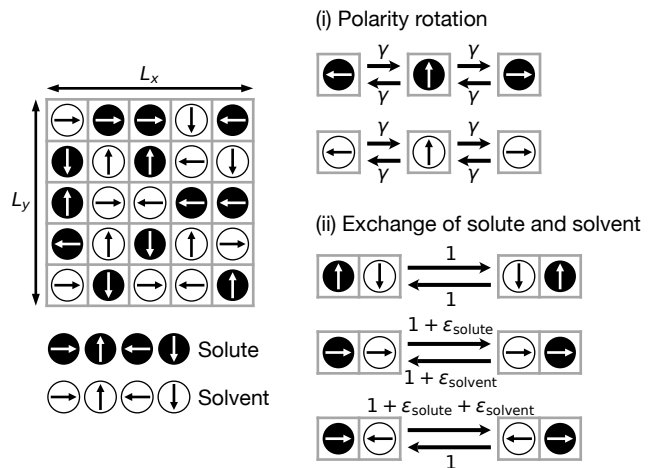


FIG. 1. Active binary mixture model. Each site of a rectangular lattice with size (L_x, L_y) is occupied by a solute with polarity (black particle with arrow) or a solvent with polarity (white particle with arrow). Each solute (solvent) stochastically (i) rotates its polarity by $\pm 90^\circ$ or (ii) exchanges its position with a neighboring solvent (solute). The polarity rotation rate is γ , and the exchange rate depends on the configuration and activity strengths, ϵ_{solute} and $\epsilon_{\text{solvent}}$.

III. BUBBLE FORMATION CONTROLLED BY ASYMMETRY OF ACTIVITY

A. Qualitative phase behavior

In Fig. 2, we show qualitative steady-state phase diagrams for active phase separation in the $(\epsilon_{\text{solute}}, \epsilon_{\text{solvent}})$ plane for $(L_x, L_y) = (100, 50)$ at (a) $\rho = 0.5$ and (b) $\rho = 0.8$. The brightness of each heatmap indicates $\Delta\rho$, the shifted difference in solute density between the dense and dilute regions, which characterizes the degree of phase separation (see Appendix A 2 for details). We also present typical snapshots at several sets of activities $(\epsilon_{\text{solute}}, \epsilon_{\text{solvent}})$ for $(L_x, L_y) = (100, 50)$ and $(L_x, L_y) = (400, 200)$.

Figure 2 suggests that phase separation is induced by solute activity and/or solvent activity. Furthermore, as represented by the snapshot at $(\epsilon_{\text{solute}}, \epsilon_{\text{solvent}}) = (10, 4)$ in Fig. 2(a), moderate asymmetry in solute and solvent activities enhances formation of solvent bubbles (shown with white color) within a large cluster of solutes (shown with black color); conversely, at $(\epsilon_{\text{solute}}, \epsilon_{\text{solvent}}) = (4, 10)$, bubbles of solutes form within a large cluster of solvents. At a higher density ($\rho = 0.8$), the snapshots in Fig. 2(b) illustrate that bubble formation is enhanced in a similar parameter region.

In Fig. 2(c), we show the time evolution of a typical configuration in the steady state at $\rho = 0.5$ and $(\epsilon_{\text{solute}}, \epsilon_{\text{solvent}}) = (10, 4)$. We find that bubbles persistently form and grow within the bulk solute-rich phase and merge into the bulk solvent-rich phase. This type of nonstationary bubble dynamics in active phase separation has also been found in active particle models [46] and coarse-grained models [39].

In the symmetric limit ($\epsilon_{\text{solute}} = \epsilon_{\text{solvent}}$), which corresponds to the diagonal line in Fig. 2, we find that bubble forma-

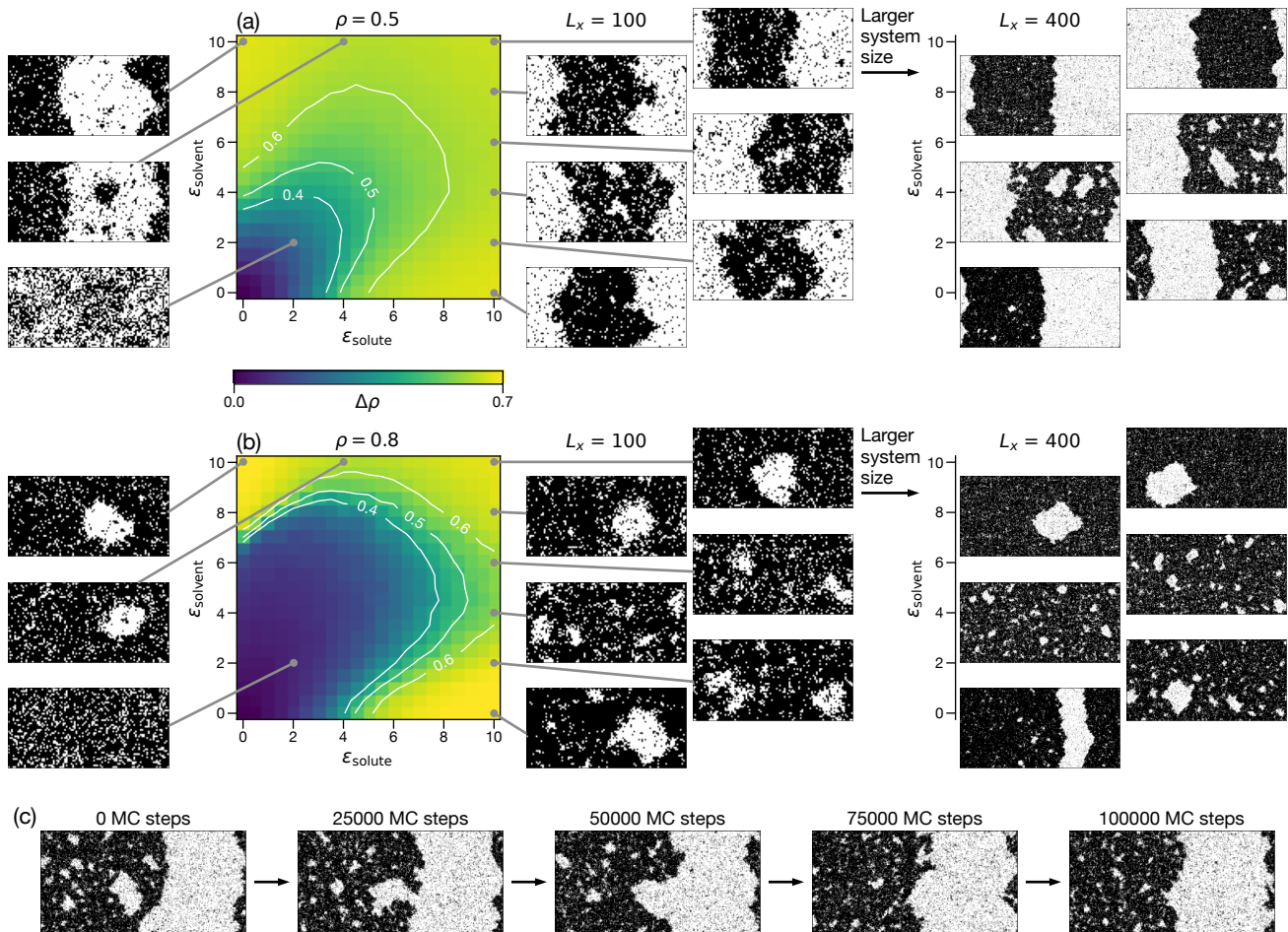


FIG. 2. Qualitative phase diagram for active phase separation. (a, b) Heatmap of $\Delta\rho$, the shifted difference in solute density between the dense and dilute regions, for $(L_x, L_y) = (100, 50)$ with (a) $\rho = 0.5$ or (b) $\rho = 0.8$. The brighter color indicates a higher degree of phase separation, and the white lines represent constant- $\Delta\rho$ lines. We show typical snapshots at several sets of activities $(\epsilon_{\text{solute}}, \epsilon_{\text{solvent}})$, where black and white colors indicate solutes and solvents, respectively. We also present several snapshots for a larger system size $[(L_x, L_y) = (400, 200)]$. (c) Typical time evolution of bubbles in the steady state. Bubbles form and grow within the bulk solute-rich phase and merge into the bulk solvent-rich phase.

tion is suppressed. This is natural since previous studies of AMB+ [33, 39, 49] indicate that the λ and ζ terms in AMB+, which correspond to effects of asymmetry between solutes and solvents in our model, are essential for bubble formation.

B. Power-law size distribution of enhanced bubbles

To examine the evolution of solvent bubbles as a function of $\epsilon_{\text{solvent}}$ more quantitatively, we consider deeply phase-separated states with large solute activity ($\epsilon_{\text{solute}} = 10$) at a fixed density ($\rho = 0.5$). We plot the bubble size distribution for a fixed system size $(L_x, L_y) = (400, 200)$ in Fig. 3(a). The vertical axis is $N_{\text{bubble}}(A)/N_{\text{solvent}}$, where $N_{\text{bubble}}(A)$ is the ensemble-averaged total number of bubbles of size A , and $N_{\text{solvent}} = (1-\rho)L_xL_y$ is the total number of solvents. The bubbles are defined as clusters of solvents, excluding the largest cluster, which is regarded as the bulk solvent-rich phase (see Appendix A 3 for details). As solvent activity increases from

$\epsilon_{\text{solvent}} = 0$ to $\epsilon_{\text{solvent}} = 6$, the bubble size distribution becomes broader [Fig. 3(a)], consistent with the enhanced bubbles observed in the snapshots [Fig. 2(a)]. Furthermore, for moderate asymmetry of activity ($\epsilon_{\text{solvent}} = 2, 4, 6$), we find an approximate power-law distribution:

$$\frac{N_{\text{bubble}}(A)}{N_{\text{solvent}}} \sim A^{-\alpha} \quad (1)$$

with $\alpha \approx 1.75$, comparable to the power-law scaling observed in simulations of active lattice gas and active Brownian particles with larger system sizes [46]. As shown in Fig. 3(b), upon increasing the system size from $(L_x, L_y) = (100, 50)$ (dotted lines) to $(L_x, L_y) = (400, 200)$ (solid lines), the distribution for $\epsilon_{\text{solvent}} = 4$ approaches the power-law scaling regime more quickly than that for $\epsilon_{\text{solvent}} = 0$ (i.e., the case equivalent to active lattice gas).

As discussed previously [46, 48], the power-law distribu-

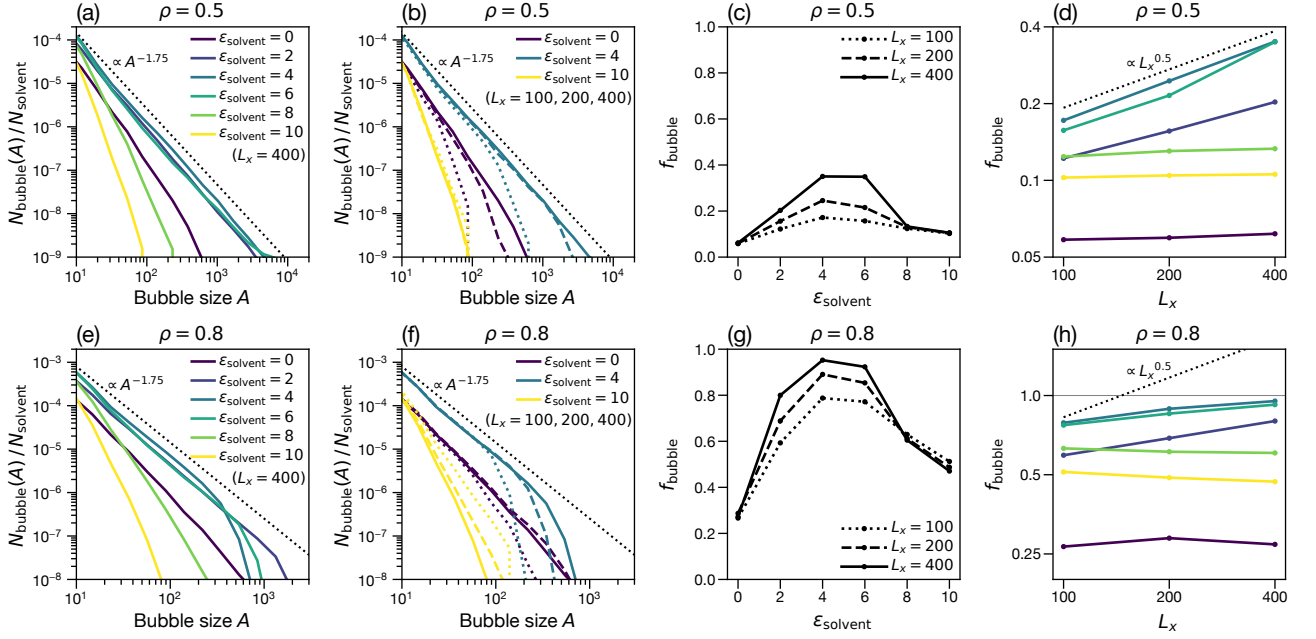


FIG. 3. Bubble formation controlled by solvent activity. (a, b) Bubble size distribution divided by the total number of solvents, $N_{\text{bubble}}(A)/N_{\text{solvent}}$, at $\rho = 0.5$ and $\epsilon_{\text{solute}} = 10$. The brightness suggests solvent activity $\epsilon_{\text{solvent}}$, and the line style indicates the system size $[(L_x, L_y) = (100, 50)$ (dotted lines), $(L_x, L_y) = (200, 100)$ (dashed lines), and $(L_x, L_y) = (400, 200)$ (solid lines)]. For moderate activity ($\epsilon_{\text{solvent}} = 2, 4, 6$) and large enough system sizes, the curves approximately follow a power-law scaling $\sim A^{-1.75}$ (black dotted line). (c, d) Bubble fraction f_{bubble} at $\rho = 0.5$ as a function of (c) $\epsilon_{\text{solvent}}$ or (d) L_x , where brightness suggests $\epsilon_{\text{solvent}}$ as in (a). For moderate $\epsilon_{\text{solvent}}$, the bubble fraction follows an approximate scaling: $f_{\text{bubble}} \sim L_x^{0.5}$ [black dotted line in (d)]. (e-h) The corresponding plots at $\rho = 0.8$ and $\epsilon_{\text{solute}} = 10$.

tion (1) with $\alpha \approx 1.75 < 2$ means that the bubble fraction,

$$f_{\text{bubble}} := \frac{1}{N_{\text{solvent}}} \sum_A A N_{\text{bubble}}(A), \quad (2)$$

should grow algebraically with L_x :

$$f_{\text{bubble}} \sim L_x^{2(2-\alpha)}, \quad (3)$$

where we assume that the aspect ratio L_x/L_y is fixed and the upper limit of the summation in Eq. (2) is proportional to $L_x L_y$ [48]. As demonstrated in Fig. 3(c), f_{bubble} is indeed enhanced for $\epsilon_{\text{solvent}} = 2, 4, 6$ as the system size increases. Moreover, as shown with the log-log plot in Fig. 3(d), f_{bubble} approximately follows the predicted scaling (3) with $2(2-\alpha) \approx 0.5$, consistent with $\alpha \approx 1.75$ in the distribution (1).

At larger solvent activities ($\epsilon_{\text{solvent}} = 8, 10$), which are comparable to the solute activity ($\epsilon_{\text{solute}} = 10$), the bubble size distribution is narrower and does not follow the power-law scaling, as shown in Fig. 3(a). This presumably reflects the suppression of bubbles by symmetry between solutes and solvents. Consistently, the bubble fraction f_{bubble} is almost independent of the system size [Figs. 3(c) and 3(d)], in contrast to the cases with moderate asymmetry ($\epsilon_{\text{solvent}} = 2, 4, 6$).

To examine the generality of the observed effects of solvent activity, we also consider systems with a higher solute density ($\rho = 0.8$) [see Fig. 2(b) for snapshots]. As shown in Figs. 3(e) and 3(f), the bubble size distribution follows the approximate power-law scaling for $\epsilon_{\text{solvent}} = 2, 4, 6$ in a similar way as observed for $\rho = 0.5$. Further, bubble formation is enhanced

for $\epsilon_{\text{solvent}} = 2, 4, 6$ as the system size increases, as suggested from Figs. 3(f) and 3(g). On the other hand, Fig. 3(h) shows that the scaling law for f_{bubble} [Eq. (3)] is violated, and f_{bubble} is almost saturated near 1 especially at $\epsilon_{\text{solvent}} = 4$. At larger solvent activities ($\epsilon_{\text{solvent}} = 8, 10$), bubbles are suppressed [Figs. 3(e)-3(h)] in a similar way as observed for $\rho = 0.5$.

Since $0 < f_{\text{bubble}} < 1$ by definition, f_{bubble} is expected to converge to a value less than or equal to 1 as $L_x L_y \rightarrow \infty$. When the power-law distribution appears in finite systems, the asymptotic phase behavior for $L_x L_y \rightarrow \infty$ should be classified into either bubbly phase separation [39, 49] ($f_{\text{bubble}} \rightarrow \text{const.} < 1$ for $L_x L_y \rightarrow \infty$) or microphase separation [39, 46] ($f_{\text{bubble}} \rightarrow 1$ for $L_x L_y \rightarrow \infty$). We need larger-scale simulations to confirm the ρ and $\epsilon_{\text{solvent}}$ dependence of the asymptotic phase behavior.

Overall, in the deeply phase-separated states caused by large solute activity, we can enhance or suppress bubble formation by moderate or large solvent activity, respectively. From symmetry, the discussions above are also applied to systems with $\epsilon_{\text{solute}} \leq \epsilon_{\text{solvent}}$ by exchanging the roles of solutes and solvents.

IV. MEAN-FIELD THEORY

To capture the observed phase behavior, particularly bubble formation, within reduced models, we employ mean-field theory [59, 63–65]. Though mean-field approximations may be

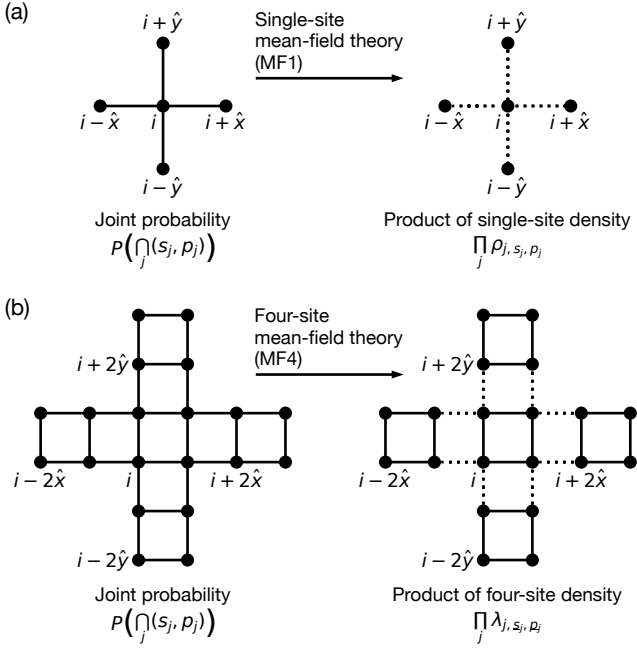


FIG. 4. Schematic explanation of (a) single-site mean-field theory and (b) four-site mean-field theory. Black dots indicate lattice sites, and dotted lines represent the neglected correlations between (a) adjacent sites or (b) adjacent clusters.

inaccurate for generic parameter regimes, they provide a useful starting point for analytical insight, especially when complemented by techniques such as linear stability analysis.

A. Single-site mean-field theory

As a simple way for model reduction, we consider single-site mean-field theory. We define $\rho_{i,s,p}(t)$ as the marginal probability that site i is occupied by species s ($\in \{\text{solute}, \text{solvent}\}$) with polarity p at time t . We can also regard $\rho_{i,s,p}(t)$ as the ensemble-averaged local density of species s with polarity p at site i and time t . As shown in Fig. 4(a), by neglecting microscopic correlations across sites in a similar way as applied previously [59, 63–65], we obtain a dynamical mean-field equation for $\rho_{i,s,p}(t)$:

$$\partial_t \rho_{i,s,p} = f_{i,s,p}^{(p)} + f_{i,s,p}^{(a)} + f_{i,s,p}^{(r)}. \quad (4)$$

The first term $f_{i,s,p}^{(p)}$ comes from the passive exchange of a solute and a solvent:

$$f_{i,s,p}^{(p)} = \sum_{l \in \{\pm \hat{x}, \pm \hat{y}\}} \sum_{p'} (\rho_{i,\bar{s},p'} \rho_{i+l,s,p} - \rho_{i+l,\bar{s},p'} \rho_{i,s,p}), \quad (5)$$

where \bar{s} suggests the species opposite to s (e.g., $\overline{\text{solute}} = \text{solvent}$), \hat{x} and \hat{y} are the unit translations in the x and y directions, respectively, and the polarity indices ($\rightarrow, \uparrow, \leftarrow, \downarrow$) are identified as $(+\hat{x}, +\hat{y}, -\hat{x}, -\hat{y})$. The second term $f_{i,s,p}^{(a)}$ derives

from the active exchange of a solute and a solvent:

$$f_{i,s,p}^{(a)} = \sum_{p'} \varepsilon_s (\rho_{i,\bar{s},p'} \rho_{i-p,s,p} - \rho_{i+p,\bar{s},p'} \rho_{i,s,p}) + \sum_{p'} \varepsilon_{\bar{s}} (\rho_{i,\bar{s},p'} \rho_{i+p',s,p} - \rho_{i-p',\bar{s},p'} \rho_{i,s,p}). \quad (6)$$

The last term $f_{i,s,p}^{(r)}$ corresponds to the rotation of polarity:

$$f_{i,s,p}^{(r)} = \gamma (\rho_{i,s,Rp} + \rho_{i,s,R^{-1}p} - 2\rho_{i,s,p}), \quad (7)$$

where R and R^{-1} represent counterclockwise and clockwise rotations by 90° , respectively [e.g., $R(+\hat{y}) = -\hat{x}$].

B. Phase behavior in mean-field dynamics

In Fig. 5(a), we present typical snapshots of the solute density, $\rho_{i,\text{solute}} := \sum_p \rho_{i,\text{solute},p}$, for $(L_x, L_y) = (100, 50)$ in the $(\varepsilon_{\text{solute}}, \varepsilon_{\text{solvent}})$ plane at $\rho = 0.5$. Each snapshot is obtained by numerical integration of Eq. (4) until $t = 2000$ using the Euler method with time step $dt = 0.02$, where the initial state is a fully phase-separated configuration with random polarity [see Fig. 9(b)]. We find that the mean-field dynamics qualitatively reproduces the enhancement of bubble formation by moderate asymmetry of activity as seen in the original model [Fig. 2(a)].

As demonstrated in Fig. 6(a) for $(\varepsilon_{\text{solute}}, \varepsilon_{\text{solvent}}) = (10, 3)$, we find that nonstationary bubble dynamics appears for a certain range of activity parameters, even though the mean-field equation [Eq. (4)] is deterministic. Bubbles persistently form and grow within the bulk solute-rich phase and merge into the bulk solvent-rich phase, in a similar way as observed in stochastic simulations of the original model [Fig. 2(c)]. We plot the corresponding bubble size distribution in Fig. 6(d) (see Appendix B 1 for details), which suggests that larger bubbles tend to appear in larger systems, as seen in the original model [Fig. 3(b)]. However, the distribution saturates at relatively small system sizes, such as $(L_x, L_y) = (200, 100)$. Also, the power laws in the distribution [i.e., $N_{\text{bubble}}(A)/N_{\text{solvent}} \sim A^{-1.75}$] and bubble fraction (i.e., $f_{\text{bubble}} \sim L_x^{0.5}$) are not so clear [Figs. 6(d) and 6(e)], compared to the observations in the original model [Figs. 3(b) and 3(d)]. Such discrepancies may come from the absence of stochasticity in the mean-field dynamics, since stochasticity should increase the nucleation rate of bubbles and affect the bubble size distribution.

To consider the mechanism of enhanced bubble formation within mean-field theory, we examine the polarity density of solutes and solvents, defined as $w_{i,s} := \sum_p p \rho_{i,s,p}$, for $(\varepsilon_{\text{solute}}, \varepsilon_{\text{solvent}}) = (10, 3)$. As illustrated by the colored arrows in Figs. 6(b) and 6(c), the polarity densities of solutes and solvents are aligned near the interface between the solute-rich and solvent-rich phases. First, the polarity of solutes is oriented toward the solute-rich phase, in a similar way as observed in phase separation of active particles [66–68]. This alignment of solute polarity derives from solute activity and exclusion, and is interpreted to stabilize the large cluster of solutes against diffusion. Second, the polarity density of solvents is also oriented toward the solute-rich phase, which re-

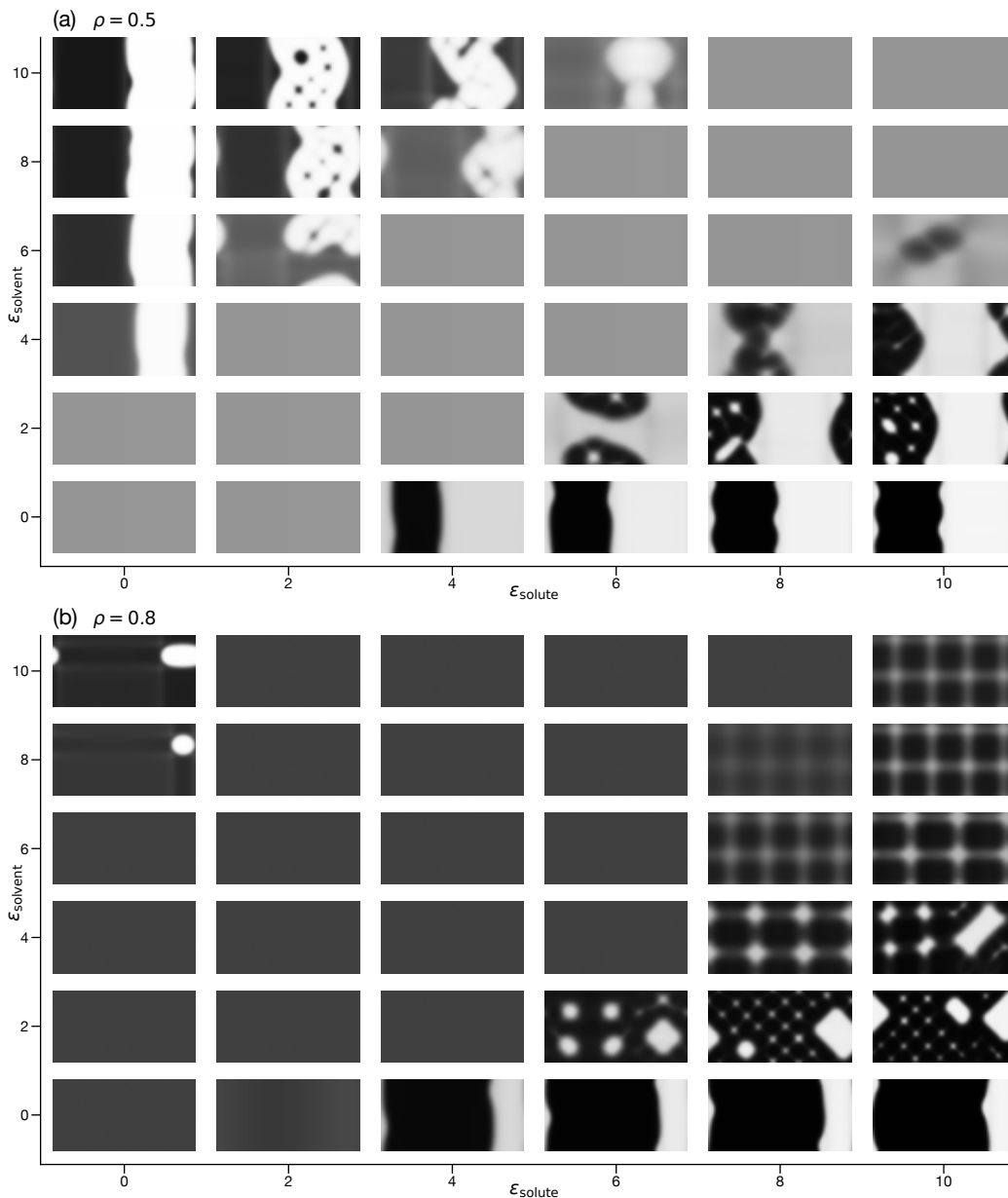


FIG. 5. Phase behavior in mean-field dynamics. (a, b) Typical snapshots for different sets of $(\epsilon_{\text{solute}}, \epsilon_{\text{solvent}})$ with $(L_x, L_y) = (100, 50)$ at (a) $\rho = 0.5$ or (b) $\rho = 0.8$. Grayscale represents solute density $\rho_{i,\text{solute}}$ (white for $\rho_{i,\text{solute}} = 0$ and black for $\rho_{i,\text{solute}} = 1$).

flects asymmetry in activity and is presumably due to the particle exchange driven by solvent activity near the interface. This alignment of solvent polarity is interpreted to expand bubbles within the solute-rich phase, leading to the enhancement of bubble formation.

In Fig. 5(b), we show typical snapshots in the case of $\rho = 0.8$. We find that bubble formation is enhanced for moderate asymmetry of activity, such as $(\epsilon_{\text{solute}}, \epsilon_{\text{solvent}}) = (10, 2)$, in a similar way as observed in the original model [Fig. 2(b)]. The periodic patterns seen in the mean-field dynamics [Fig. 5(b)] suggest the propensity for microphase separation at high density, though bubbles exhibit more fluctuating behaviors in the original stochastic model [Fig. 2(b)].

The mean-field dynamics does not reproduce macroscopic phase separation near the symmetric limit ($\epsilon_{\text{solute}} = \epsilon_{\text{solvent}}$), which is observed in the original model [Figs. 2(a) and 2(b)]; only the homogeneous state appears for $\rho = 0.5$ [Fig. 5(a)], and the homogeneous state or periodic pattern appears for $\rho = 0.8$ [Fig. 5(b)]. This indicates a qualitative shortcoming in single-site mean-field theory. In particular, for $\rho = 0.5$, a critical point for macroscopic phase separation should exist on the line $\epsilon_{\text{solute}} = \epsilon_{\text{solvent}}$, highlighting the need to refine mean-field theory, which we conduct in Sec. IV D.

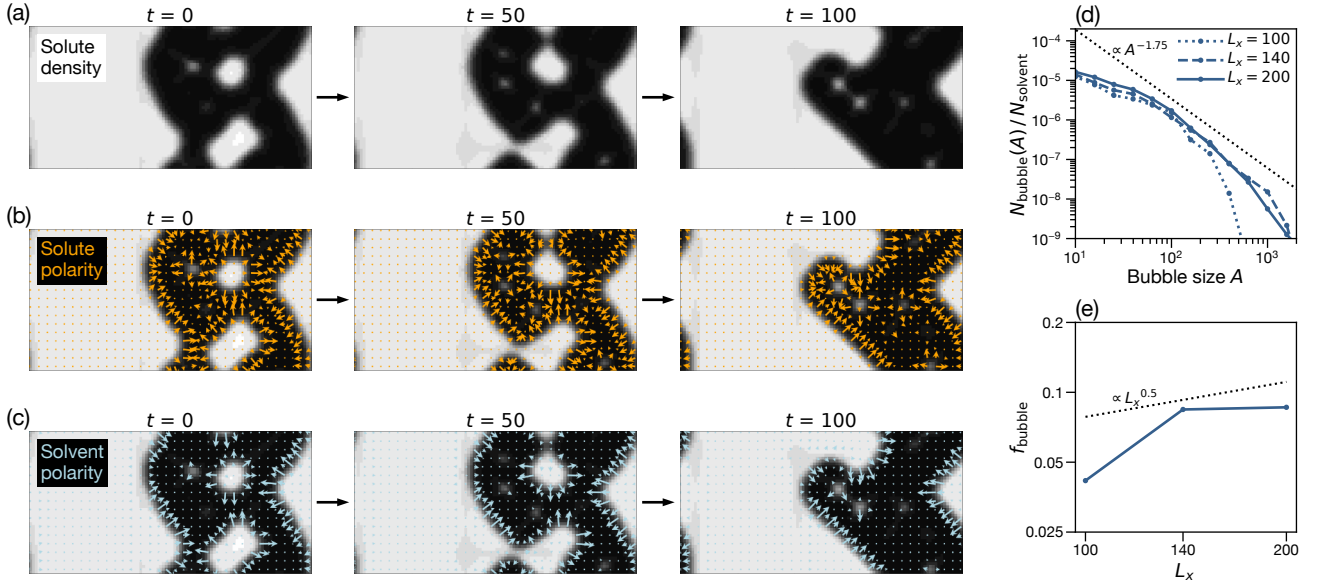


FIG. 6. Nonstationary bubble formation in mean-field dynamics. (a-c) Typical time evolution of bubbles. Grayscale indicates solute density $\rho_{i,\text{solute}}$. Arrows in (b) orange and (c) light blue represent solute polarity density $w_{i,\text{solute}}$ and solvent polarity density $w_{i,\text{solvent}}$, respectively, shown in arbitrary units. (d) Bubble size distribution divided by the total number of solvents, $N_{\text{bubble}}(A)/N_{\text{solvent}}$, for three system sizes $[(L_x, L_y) = (100, 50), (140, 70), (200, 100)]$, shown with a power-law function $\propto A^{-1.75}$ (black dotted line). (e) Bubble fraction f_{bubble} , shown with a power-law function $\propto L_x^{0.5}$ (black dotted line). For all panels, we set $\rho = 0.5$ and $(\varepsilon_{\text{solute}}, \varepsilon_{\text{solvent}}) = (10, 3)$.

C. Linear stability analysis

Motivated by the mean-field dynamics reproducing the enhancement of bubbles by moderate activity asymmetry, we apply linear stability analysis to Eq. (4) around the homogeneous state [i.e., $\rho_{i,\text{solute},p} = \rho/4$ and $\rho_{i,\text{solvent},p} = (1-\rho)/4$ for any i or p]. From Eq. (4), we derive the linearized dynamical equation for the Fourier mode of fluctuations, $\rho_k(t)$:

$$\partial_t \rho_k = R_k^{\text{MF1}} \rho_k. \quad (8)$$

Here, ρ_k is an 8-dimensional vector ($[\rho_k]_{s,p} := \rho_{k,s,p} := \sum_j e^{-ik \cdot j} \rho_{j,s,p}$), and R_k^{MF1} is an 8×8 matrix (see Appendix B 2 for details).

Since $\sum_{s,p} \rho_{k,s,p} = 0$ holds for each k , which is derived from $\sum_{s,p} \rho_{i,s,p} = 1$ for any i , the total number of independent variables in Eq. (8) is 7 for each k . Thus, R_k^{MF1} has one trivial zero eigenvalue for each k . After excluding this zero eigenvalue, we define r_k^{MF1} as the eigenvalue of R_k^{MF1} with the largest real part. If $\text{Re } r_k^{\text{MF1}} > 0$ for some k , the homogeneous state is unstable against fluctuation with wavevector k . On the other hand, if $\text{Re } r_k^{\text{MF1}} < 0$ for any $k \neq \mathbf{0}$, the homogeneous state is linearly stable. Note that $r_0^{\text{MF1}} = 0$ always holds due to the particle number conservation (i.e., $\sum_{i,p} \rho_{i,\text{solute},p} = \rho L^2$).

In Fig. 7(b), we show the spinodal line (i.e., stability limit of the homogeneous state) in the $(\varepsilon_{\text{solute}}, \varepsilon_{\text{solvent}})$ plane at $\rho = 0.8$. To obtain the spinodal line, at

which $\max_k \text{Re } r_k^{\text{MF1}}$ shifts from zero to a positive value, we numerically maximized $\text{Re } r_k^{\text{MF1}}$ with a Python package (`scipy.optimize.differential_evolution` [69]) using the default parameters. We find two regions of the spinodal line: one toward macroscopic phase separation (i.e., instability with $k \rightarrow \mathbf{0}$, shown with a black solid line), and the other toward microphase separation (i.e., instability with $k \neq \mathbf{0}$, shown with a blue dashed line). These two regions merge at the Lifshitz point [70], indicated by a blue dot. For comparison, we also show the constant- $\Delta\rho$ lines reproduced from Fig. 2(b) with gray thin lines. The results suggest that the tendency toward microphase separation induced by solvent activity is explained by linear instability, and the constant- $\Delta\rho$ lines (i.e., transition lines) are qualitatively captured by the spinodal line. Note that the spinodal lines do not follow the constant- $\Delta\rho$ lines on the upper side in the $(\varepsilon_{\text{solute}}, \varepsilon_{\text{solvent}})$ plane, where the transition can happen only through nucleation, which cannot be explained by linear stability analysis.

To gain further insight into microphase separation caused by solvent activity, we focus on the functional dependence of r_k^{MF1} on $\varepsilon_{\text{solute}}$, $\varepsilon_{\text{solvent}}$, and ρ . With the adiabatic approximation for fast variables [71, 72] and an assumption that the diagonal modes (i.e., $k_x = \pm k_y$) are most unstable (see Appendix B 2 for details), we obtain the analytical expression of r_k^{MF1} for small wavenumber $|k|$:

$$r_k^{\text{MF1}} = c_2^{\text{MF1}} |k|^2 + c_{4+}^{\text{MF1}} |k|^4 + O(|k|^6), \quad (9)$$

where

$$c_2^{\text{MF1}} = -\left(1 + \frac{\varepsilon_{\text{solute}} + \varepsilon_{\text{solvent}}}{4}\right) + \frac{\varepsilon_{\text{solute}}^2(1-\rho)(2\rho-1)}{4\gamma} - \frac{\varepsilon_{\text{solvent}}^2\rho(2\rho-1)}{4\gamma}, \quad (10)$$

$$c_{4+}^{\text{MF1}} = \frac{1}{24}\left(1 + \frac{\varepsilon_{\text{solute}} + \varepsilon_{\text{solvent}}}{4}\right) - \frac{\varepsilon_{\text{solute}}^2(1-\rho)(2\rho-1)}{24\gamma} + \frac{\varepsilon_{\text{solvent}}^2\rho(2\rho-1)}{24\gamma} - \frac{\varepsilon_{\text{solute}}^2}{8\gamma^2}\left(1 + \frac{\varepsilon_{\text{solute}} + \varepsilon_{\text{solvent}}}{4}\right)(1-\rho)^2(2\rho-1) + \frac{\varepsilon_{\text{solvent}}^2}{8\gamma^2}\left(1 + \frac{\varepsilon_{\text{solute}} + \varepsilon_{\text{solvent}}}{4}\right)\rho^2(2\rho-1). \quad (11)$$

The spinodal line for macroscopic phase separation [black solid line in Fig. 7(b)] corresponds to the condition for $c_2^{\text{MF1}} = 0$, and the Lifshitz point [blue dot in Fig. 7(b)] is determined by $c_2^{\text{MF1}} = 0$ and $c_{4+}^{\text{MF1}} = 0$.

The expression of c_2^{MF1} [Eq. (10)] suggests distinct effects of solute and solvent activities. The first term indicates that both solute and solvent activities linearly increase the effective diffusion constant, stabilizing the homogeneous state. In contrast, the second and third terms highlight the opposite effects of solute and solvent activities at the quadratic order; for $0.5 < \rho < 1$, the solute activity $\varepsilon_{\text{solute}}$ increases c_2^{MF1} and tends to induce instability toward macroscopic phase separation, while the solvent activity $\varepsilon_{\text{solvent}}$ decreases c_2^{MF1} and stabilizes the homogeneous state; for $0 < \rho < 0.5$, the roles of solute and solvent activities are reversed. Such competition of solute and solvent activities causes the positive slope of the spinodal line in Fig. 7(b).

The expression of c_{4+}^{MF1} [Eq. (11)] illuminates further interplay of solute and solvent activities. For $0.5 < \rho < 1$, the nonlinear contribution of $\varepsilon_{\text{solvent}}$ shifts c_{4+}^{MF1} toward positive values as $\varepsilon_{\text{solvent}}$ increases. This demonstrates that solvent activity can induce microphase separation (i.e., instability with $\mathbf{k} \neq \mathbf{0}$), given that solvent activity concurrently decreases c_2^{MF1} and suppresses macroscopic phase separation as explained above. For $0 < \rho < 0.5$, the roles of solute and solvent activities are reversed.

Although linear stability analysis qualitatively accounts for the phase behavior at $\rho = 0.8$, it fails to predict a spinodal line at $\rho = 0.5$. Specifically, Eq. (10) leads to $c_2^{\text{MF1}} < 0$ for $\rho = 0.5$ regardless of $(\varepsilon_{\text{solute}}, \varepsilon_{\text{solvent}})$, and we numerically confirmed that $\text{Re} r_k^{\text{MF1}} < 0$ for any $\mathbf{k} \neq \mathbf{0}$, indicating that the homogeneous state would remain linearly stable. This contradicts the presumed existence of the critical point for macroscopic phase separation and an accompanying spinodal line, which motivates us to improve mean-field theory (Sec. IV D), as already mentioned at the end of Sec. IV B.

D. Four-site mean-field theory

To find the presumed critical point and an accompanying spinodal line for $\rho = 0.5$, we refine the mean-field theory. Instead of the approximation used in Sec. IV A, where all the microscopic correlations between neighboring sites are neglected, we incorporate local correlations at the four-site level by considering the four-site density $\lambda_{i,s,p}(t)$. Here,

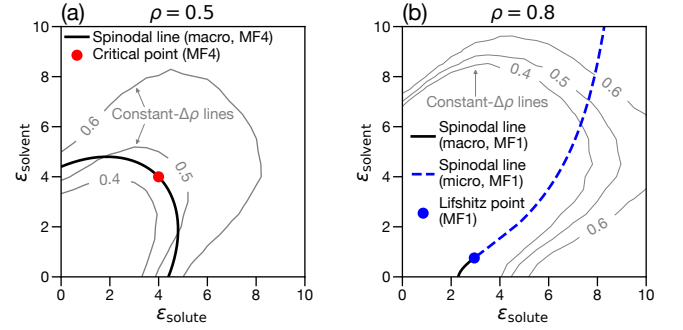


FIG. 7. Mean-field spinodal line and critical point. (a) Spinodal line (black solid line) and critical point (red dot) for macroscopic phase separation at $\rho = 0.5$, obtained by four-site mean-field theory. (b) Spinodal line for macroscopic phase separation (black solid line) or microphase separation (blue dashed line) and the Lifshitz point (blue dot) at $\rho = 0.8$, obtained by single-site mean-field theory. In each panel, the constant- $\Delta\rho$ lines (gray thin lines) are reproduced from Fig. 2 for reference.

$\underline{s} := (s_1, s_2, s_3, s_4)$ and $\underline{p} := (p_1, p_2, p_3, p_4)$ represent the configuration for a square cluster that consists of $i_1 := i$, $i_2 := i + \hat{x}$, $i_3 := i + \hat{x} + \hat{y}$, and $i_4 := i + \hat{y}$, which we call cluster i . More specifically, $\lambda_{i,s,p}(t)$ is the marginal joint probability that site i_n is occupied by species s_n with polarity p_n for $n \in \{1, 2, 3, 4\}$ at time t . In this subsection, we assume that L_x and L_y are even numbers, and the x and y coordinates of site i are odd numbers.

We derive the dynamical mean-field equation for $\lambda_{i,s,p}(t)$ by neglecting the correlations across square clusters [Fig. 4(b)]:

$$\partial_t \lambda_{i,s,p} = g_{i,s,p}^{(p,w)} + g_{i,s,p}^{(a,w)} + g_{i,s,p}^{(p,n)} + g_{i,s,p}^{(a,n)} + g_{i,s,p}^{(r)}. \quad (12)$$

Here, $g_{i,s,p}^{(p,w)}$ is the contribution from the passive exchange within cluster i (e.g., exchange of solute with polarity $+\hat{y}$ at site i and solvent with polarity $-\hat{y}$ at site $i + \hat{x}$). Similarly, $g_{i,s,p}^{(a,w)}$ is the contribution from the active exchange within cluster i (e.g., exchange of solute with polarity $+\hat{x}$ at site i and solvent with polarity $-\hat{y}$ at site $i + \hat{x}$). Next, $g_{i,s,p}^{(p,n)}$ and $g_{i,s,p}^{(a,n)}$ correspond to the passive and active exchanges, respectively, across cluster i and neighboring clusters (e.g., active exchange of solute with polarity $-\hat{x}$ at site i and solvent with polarity $+\hat{y}$ at site $i - \hat{x}$). Lastly, $g_{i,s,p}^{(r)}$ represents the rotation of polarity within cluster i . The explicit form of Eq. (12) is summarized in Appendix B 3.

In a similar way as used in Sec. IV C, we first linearize Eq. (12) in terms of the fluctuations of $\lambda_{i,\underline{s},p}$ around the homogeneous state, which is determined by solving Eq. (12) numerically under the assumption that $\lambda_{i,\underline{s},p}$ is spatially uniform (i.e., independent of i). Then, using $\lambda_{k,\underline{s},p}$, the Fourier component of fluctuations with wavevector \mathbf{k} , we obtain the linearized equation in the following form:

$$\partial_t \lambda_{\mathbf{k}} = R_{\mathbf{k}}^{\text{MF4}} \lambda_{\mathbf{k}}. \quad (13)$$

Here, $\lambda_{\mathbf{k}}$ is a 4096-dimensional vector ($[\lambda_{\mathbf{k}}]_{\underline{s},p} := \lambda_{k,\underline{s},p}$), and $R_{\mathbf{k}}^{\text{MF4}}$ is a 4096 \times 4096 matrix, considering that the total number of combinations of $(\underline{s}, \underline{p}) = (s_1, s_2, s_3, s_4, p_1, p_2, p_3, p_4)$ is $2^4 \times 4^4 = 4096$.

Since $\sum_{\underline{s},p} \lambda_{k,\underline{s},p} = 0$ holds for each \mathbf{k} , which is derived from $\sum_{\underline{s},p} \lambda_{i,\underline{s},p} = 1$ for any i , the total number of independent variables in Eq. (13) is 4095 for each \mathbf{k} . Thus, $R_{\mathbf{k}}^{\text{MF4}}$ has one trivial zero eigenvalue for each \mathbf{k} . After excluding this zero eigenvalue, we define $r_{\mathbf{k}}^{\text{MF4}}$ as the eigenvalue of $R_{\mathbf{k}}^{\text{MF4}}$ with the largest real part. In the same way as explained for $r_{\mathbf{k}}^{\text{MF4}}$, the homogeneous state is unstable if $\text{Re } r_{\mathbf{k}}^{\text{MF4}} > 0$ for some \mathbf{k} , while the homogeneous state is linearly stable if $\text{Re } r_{\mathbf{k}}^{\text{MF4}} < 0$ for any $\mathbf{k} \neq \mathbf{0}$.

Examining $r_{\mathbf{k}}^{\text{MF4}}$ for $\rho = 0.5$ numerically, we obtain the spinodal line for macroscopic phase separation, as shown with a black line in Fig. 7(a). We also identify the critical point on the diagonal line (i.e., $\varepsilon_{\text{solute}} = \varepsilon_{\text{solvent}}$), which is marked by a red dot in Fig. 7(a). First, the spinodal line based on four-site mean-field theory has a positive slope near $\varepsilon_{\text{solvent}} = 0$. This suggests the competition between solute and solvent activities, as discussed more explicitly for $\rho \neq 0.5$ within single-site mean-field theory (Sec. IV C). Second, the spinodal line reproduces the qualitative feature of the constant- $\Delta\rho$ lines [gray thin lines in Fig. 7(a)], in contrast to single-site mean-field theory, which fails to predict linear instability at $\rho = 0.5$. This suggests that local correlations, which are incorporated in four-site mean-field theory but are discarded in single-site mean-field theory, should be crucial to the critical phase separation.

At $\rho = 0.5$ in the symmetric limit ($\varepsilon_{\text{solute}} = \varepsilon_{\text{solvent}} = \varepsilon$), the critical point activity is obtained numerically as $\varepsilon_c^{\text{MF4}} \simeq 4.00$, and phase separation is predicted to appear when $\varepsilon > \varepsilon_c^{\text{MF4}}$. We expect that $\varepsilon_c^{\text{MF4}}$ quantitatively deviates from the exact critical point because the latter accounts for correlations spanning all length scales rather than being limited to the four-site correlations. More importantly, the correlations at large length scales can shift the critical exponents from their mean-field values to those in a specific universality class [70, 73], which we discuss in Sec. V.

Single-site mean-field	Four-site mean-field	Numerical
–	$\varepsilon_c^{\text{MF4}} \simeq 4.00$	$\varepsilon_c = 5.262(2)$

TABLE I. Comparison of the critical point activity obtained by four-site mean-field theory ($\varepsilon_c^{\text{MF4}}$) and numerical simulations (ε_c). Single-site mean-field theory does not predict the critical point.

V. CRITICALITY UNDER BUBBLE SUPPRESSION

In this section, we set $\rho = 0.5$ and consider the symmetric limit ($\varepsilon_{\text{solute}} = \varepsilon_{\text{solvent}} = \varepsilon$). With this setup, the critical phase separation should appear on increasing activity ε , according to the symmetry of the model (Sec. II) and four-site mean-field theory (Sec. IV D). Bubble formation has been thought to influence the critical behavior in active phase separation, potentially causing the critical exponents to deviate from the Ising universality class [33, 44, 46, 51]. Since bubbles are suppressed under the symmetric limit (Sec. III), we expect to determine the critical exponents for active phase separation with negligible influence from bubbles.

We consider rectangular systems with a fixed aspect ratio ($L_x/L_y = 2$), where phase separation tends to appear along the x axis. Then, we define the order parameter for phase separation:

$$\hat{\phi} := \frac{\sin(\pi/L_x)}{L_y} \left| \sum_{j,p} e^{-2\pi i j_x/L_x} n_{j,\text{solute},p} \right|, \quad (14)$$

where j_x is the x coordinate of site j , and $n_{j,\text{solute},p}$ is the local solute occupancy: $n_{j,\text{solute},p} = 1$ if site j is occupied by a solute with polarity p and $n_{j,\text{solute},p} = 0$ otherwise. The prefactor is introduced so that $\hat{\phi} = 1$ for configurations that correspond to full phase separation along the x axis. Note that $\langle \hat{\phi}^2 \rangle$ is proportional to the longest-wavelength component of the structure factor, $S(k_x = 2\pi/L_x, k_y = 0)$, where $\langle \dots \rangle$ is the ensemble average in the steady state. Order parameters similar to Eq. (14) have been used in numerical studies of anisotropic phase separation in driven lattice gas models [74, 75] and active particle models [48, 76].

To obtain the critical point ε_c and critical exponents (ν, β, γ), we perform the finite-size scaling analysis [77] based on the scaling hypothesis: $\langle \hat{\phi}^n \rangle(\varepsilon, L_x) = L_x^{-n\beta/\nu} F_n(L_x^{1/\nu}(\varepsilon - \varepsilon_c))$ for $\varepsilon \simeq \varepsilon_c$ and $n \geq 1$, where F_n is a scaling function. We take the Binder ratio $Q := \langle \hat{\phi}^2 \rangle^2 / \langle \hat{\phi}^4 \rangle$, the (ensemble-averaged) order parameter $\phi := \langle \hat{\phi} \rangle$, and the susceptibility $\chi := L_x L_y (\langle \hat{\phi}^2 \rangle - \langle \hat{\phi} \rangle^2)$ as observables. According to the scaling hypothesis, these observables should follow

$$Q(\varepsilon, L_x) = \tilde{Q}(L_x^{1/\nu}(\varepsilon - \varepsilon_c)), \quad (15)$$

$$\phi(\varepsilon, L_x) = L_x^{-\beta/\nu} \tilde{\phi}(L_x^{1/\nu}(\varepsilon - \varepsilon_c)), \quad (16)$$

$$\chi(\varepsilon, L_x) = L_x^{\gamma/\nu} \tilde{\chi}(L_x^{1/\nu}(\varepsilon - \varepsilon_c)), \quad (17)$$

where \tilde{Q} , $\tilde{\phi}$, and $\tilde{\chi}$ are scaling functions. Though the scaling hypothesis suggests the relation $2\beta/\nu + \gamma/\nu = 2$, we estimate ($\nu, \beta/\nu, \gamma/\nu$) as independent parameters from the data for $Q(\varepsilon, L_x)$, $\phi(\varepsilon, L_x)$, and $\chi(\varepsilon, L_x)$, which are obtained from steady-state configurations for several system sizes ($L_x = 70, 100, 140, 200, 280$ with $L_x/L_y = 2$) (see Appendix A 4 for details of sampling configurations). If the critical exponents belong to the two-dimensional Ising universality class, we expect $\nu = \nu_{\text{Ising}} := 1$, $\beta = \beta_{\text{Ising}} := 0.125$, and $\gamma = \gamma_{\text{Ising}} := 1.75$ [58].

In Fig. 8(a), we plot the Binder ratio $Q(\varepsilon, L_x)$ as a function of ε for different system sizes. We find that $Q(\varepsilon, L_x)$ shows

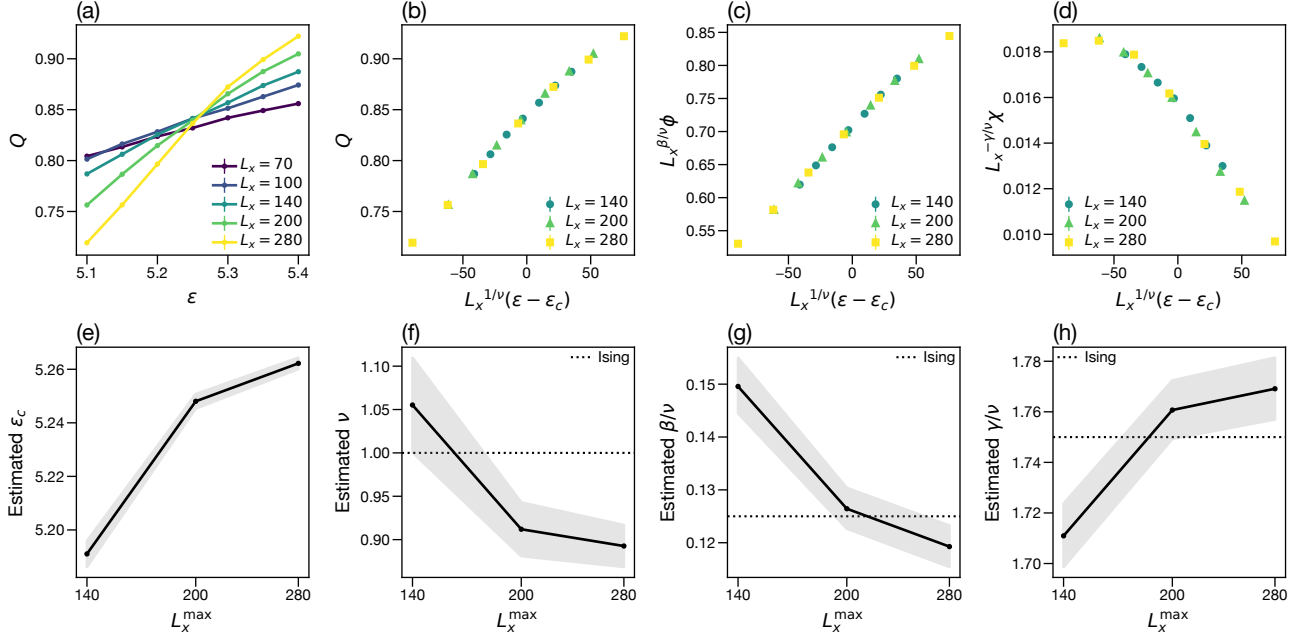


FIG. 8. Supposed Ising universality of critical phenomena for active phase separation in the symmetric limit ($\varepsilon_{\text{solute}} = \varepsilon_{\text{solvent}} = \varepsilon$). (a) Binder ratio Q as a function of activity ε for different system sizes with fixed $L_x/L_y = 2$. (b-d) Rescaled plots of the (b) Binder ratio Q , (c) order parameter ϕ , and (d) susceptibility χ , based on the finite-size scaling hypothesis [Eqs. (15)-(17)] for the three largest system sizes. (e) Estimated critical point ε_c as a function of L_x^{max} , the maximum L_x in the data set used for fitting. (f-h) Estimated critical exponents (ν , β/ν , and γ/ν) as a function of L_x^{max} , where the dotted lines suggest the Ising critical exponents. In (e-h), the estimation error is indicated by shading.

approximate crossing for $L_x \geq 100$. The crossing point is expected to coincide with the critical point ε_c since $Q(\varepsilon, L_x)$ should be independent of L_x at $\varepsilon = \varepsilon_c$, i.e., $Q(\varepsilon = \varepsilon_c, L_x) = \tilde{Q}(0)$, according to Eq. (15).

To determine ε_c and ν , we performed nonlinear least squares fitting of the data for $Q(\varepsilon, L_x)$ using a polynomial function. Fitting was applied to each data set with three sequential system sizes (i.e., $L_x \in \{70, 100, 140\}$, $\{100, 140, 200\}$, or $\{140, 200, 280\}$) to visualize higher-order corrections to the finite-size scaling hypothesis [78] (see Appendix A 4 b for details). Please refer to Appendix A 4 c for validation of the same procedure within the equilibrium lattice gas model, which is known to show the Ising critical exponents [58].

In Figs. 8(e) and 8(f), we plot the estimated values of ε_c and ν along with their estimation errors (indicated by shading) as a function of L_x^{max} , the maximum L_x in the used data set. For the data set with the largest L_x^{max} ($= 280$), the estimated exponent, $\nu = 0.89(2)$, is reasonably close to the Ising critical exponent, $\nu_{\text{Ising}} = 1$, where the value in parentheses represents the error in the last significant digit. In addition, the estimated critical point activity, $\varepsilon_c = 5.262(2)$, is larger than $\varepsilon_c^{\text{MF4}} \simeq 4.00$ obtained by four-site mean-field theory (Sec. IV D) as summarized in Table I, suggesting that long-range correlations beyond the four-site level make the homogeneous state more robust against activity.

We applied similar fitting procedures to the data for the order parameter $\phi(\varepsilon, L_x)$ and susceptibility $\chi(\varepsilon, L_x)$ to estimate β/ν and γ/ν , respectively (see Appendix A 4 b for details). In

Figs. 8(g) and 8(h), we plot the obtained values of β/ν and γ/ν with their estimation errors as a function of L_x^{max} . For the data set with the largest L_x^{max} ($= 280$), the estimated values [$\beta/\nu = 0.119(4)$ and $\gamma/\nu = 1.77(1)$] are close to the Ising counterparts ($\beta_{\text{Ising}}/\nu_{\text{Ising}} = 0.125$ and $\gamma_{\text{Ising}}/\nu_{\text{Ising}} = 1.75$). With the obtained critical exponents, we present the rescaled plots for Q , ϕ , and χ in Figs. 8(b)-8(d). Each plot suggests that the curves for different system sizes follow the universal scaling form, as expected from the scaling hypothesis [Eqs. (15)-(17)].

The estimated critical exponents [$\nu = 0.89(2)$, $\beta/\nu = 0.119(4)$, and $\gamma/\nu = 1.77(1)$] are comparable to the Ising critical exponents ($\nu_{\text{Ising}} = 1$, $\beta_{\text{Ising}}/\nu_{\text{Ising}} = 0.125$, and $\gamma_{\text{Ising}}/\nu_{\text{Ising}} = 1.75$), we argue that critical phenomena for active phase separation under bubble suppression belong to the Ising universality class, though finite-size effects still remain in estimation [Figs. 8(e)-8(h)]. This is consistent with the prediction by perturbative renormalization group analyses of coarse-grained models in the regime of macroscopic phase separation [44, 52].

VI. SUMMARY AND OUTLOOK

In this paper, we have proposed an active binary mixture model, where we have found that bubble formation in active phase separation is controlled by the asymmetry in activities of solute and solvent ($\varepsilon_{\text{solute}}$ and $\varepsilon_{\text{solvent}}$). With moderate activity asymmetry ($\varepsilon_{\text{solvent}} \sim \varepsilon_{\text{solute}}/2$), we have found that the

power-law scaling of the bubble size distribution is accessible in relatively small systems, compared to the active lattice gas limit ($\varepsilon_{\text{solvent}} = 0$). By employing mean-field theory that reproduces essential phase behaviors, we have discussed the potential mechanism for the bubble formation enhanced by activity asymmetry, as well as the competition of solute and solvent activities. Furthermore, in the symmetric limit ($\varepsilon_{\text{solvent}} = \varepsilon_{\text{solute}}$), where bubbles are suppressed, numerical investigations have indicated that the critical phenomena of active phase separation belong to the Ising universality class.

Bubbles have been suspected to change the critical exponents for active phase separation from the Ising critical exponents [33, 44, 46, 51]. By enhancing the bubble formation within our model, we can potentially investigate this effect using relatively small system sizes, thereby reducing computational cost. In addition, the mean-field dynamics [Eq. (4)], supplemented with noise, may provide another framework for examining the critical dynamics with bubble formation.

The controllability of bubbles by activity asymmetry may be observed in other active particle systems, such as a binary mixture of active Brownian particles [79]. More broadly, introducing solvent activity in active particle models will be interesting to study active matter phases in terms of symmetry between dense and dilute phases, given that phase separation appears ubiquitously [25], e.g., in flocking [63, 64, 80] or active nematics [81].

ACKNOWLEDGMENTS

We thank Kyogo Kawaguchi and Hiroyoshi Nakano for their continuous discussions and insightful comments. We also thank Hugues Chaté and Kiyoshi Kanazawa for invaluable comments. We acknowledge support by the RIKEN Information systems division for the use of the Supercomputer HOKUSAI BigWaterfall2. This work was supported by JSPS KAKENHI Grant Number JP20K14435.

Appendix A: Numerical simulations

1. Implementation of stochastic dynamics

We consider two types of initial configurations: (a) “random initial state”, in which both position and polarity of each particle are randomly chosen [Fig. 9(a)], and (b) “separated initial state”, in which solutes and solvents are fully segregated along the x axis, but polarity of each particle is randomly chosen [Fig. 9(b)]. The random initial states were used to examine critical phenomena (Fig. 8), while the separated initial states were used to examine the phase diagram (Fig. 2) and bubble formation (Fig. 3).

To implement the stochastic dynamics of the lattice model (Fig. 1), we discretize the time with interval Δt . In a single Monte Carlo (MC) step, we update the configuration as follows:

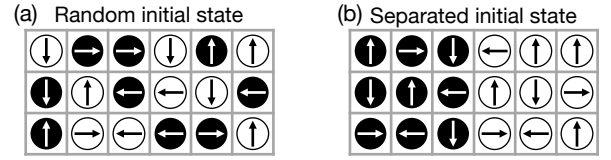


FIG. 9. Two types of initial configurations. (a) Example of a random initial state. (b) Example of a separated initial state. The color and arrow indicate the species and polarity, respectively, in the same way as used in Fig. 1.

- (1) We randomly choose a particle, regardless of its species (i.e., solute or solvent).
- (2) The chosen particle (of species s with polarity p at site i) (i) rotates its polarity or (ii) exchanges its position with one of the neighboring particles with the following probabilities.
 - (i) The polarity p rotates by $+90^\circ$ or -90° , each with probability $\gamma\Delta t$.
 - (ii) For each direction $l \in \{+\hat{x}, +\hat{y}, -\hat{x}, -\hat{y}\}$, if the species s is distinct from the species s' of the particle at site $i+l$ (with polarity p'), the positions of these two particles are exchanged with probability $(1 + \varepsilon_s\delta_{p,l} + \varepsilon_{s'}\delta_{p',-l})\Delta t/2$. Here, \hat{x} and \hat{y} are the unit translations in the x and y directions, respectively, and the polarity indices ($\rightarrow, \uparrow, \leftarrow, \downarrow$) are identified as $(+\hat{x}, +\hat{y}, -\hat{x}, -\hat{y})$, and $\delta_{a,b}$ is the Kronecker delta. Note that the factor $1/2$ appears in the exchange probability to compensate for the double counting of the same trial when selecting the particle at $i+l$ in procedure (1).
- (3) We repeat procedures (1) and (2) $L_x L_y$ times and increment the time by Δt .

To minimize the rejection probability in each trial, we set

$$\Delta t = \frac{1}{(4 + \varepsilon_{\text{solute}} + \varepsilon_{\text{solvent}} + 3 \max\{\varepsilon_{\text{solute}}, \varepsilon_{\text{solvent}}\})/2 + 2\gamma} \quad (\text{A1})$$

in all the simulations conducted in this study.

See Ref. [82] for sample simulation codes, which can be executed on Google Colab to generate simulation videos.

2. Qualitative phase diagram

We define the most dense and dilute regions as the square subsystems (of size $L_0 \times L_0$) that contain the maximum and minimum number of solutes, respectively. For a given configuration at certain activities ($\varepsilon_{\text{solute}}, \varepsilon_{\text{solvent}}$), we define $\Delta\hat{\rho}'$ as the difference in solute density between the most dense and dilute regions. Writing the ensemble average of $\Delta\hat{\rho}'$ as $\Delta\rho'$, we define the shifted density difference as

$$\Delta\rho := \Delta\rho' - \Delta\rho'_0, \quad (\text{A2})$$

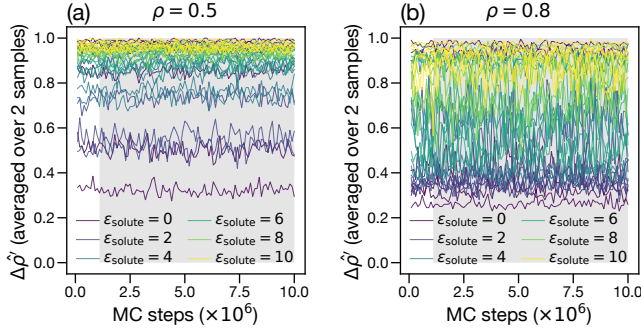


FIG. 10. Time evolution of $\Delta\rho'$. (a, b) Time-dependent $\Delta\rho'$ for different sets of $(\varepsilon_{\text{solute}}, \varepsilon_{\text{solvent}})$, where the brightness suggests the solute activity, at (a) $\rho = 0.5$ or (b) $\rho = 0.8$. In (a) and (b), the gray area indicates the time points used for averaging to produce Figs. 2(a) and 2(b), respectively.

where $\Delta\rho'_0$ is the value of $\Delta\rho'$ at $\varepsilon_{\text{solute}} = \varepsilon_{\text{solvent}} = 0$ (i.e., baseline with no spatial correlation).

To plot the qualitative phase diagram for systems with $(L_x, L_y) = (100, 50)$ (Fig. 2), we used $L_0 = 10$ and obtained $\Delta\rho'$ as the average of $\Delta\rho'$ over two independent samples with 90 time points each, taken every 10^5 MC steps after relaxation with 10^6 MC steps using the separated initial state [Fig. 9(b)]. The time evolution of $\Delta\rho'$ averaged over two independent samples for several values of $(\varepsilon_{\text{solute}}, \varepsilon_{\text{solvent}})$ is plotted in Fig. 10, where the gray area indicates the time points used for averaging.

Since the value of $\Delta\rho$ depends on L_0 , we checked how the constant- $\Delta\rho$ lines depend on L_0 . In Fig. 11, we show the change in the heatmap of $\Delta\rho$ when L_0 increases as $L_0 = 10, 15, 20$, which suggests that the qualitative feature of the constant- $\Delta\rho$ lines is similar regardless of the specific value of L_0 .

3. Bubble formation

For each configuration, we define the bubbles as clusters of solvents, excluding the largest cluster, which is regarded as the bulk solvent-rich phase. The bubble clusters are obtained using a Python package (`scipy.ndimage.label` [69]) with the default connectivity parameter (i.e., the nearest neighbors regarded as connected).

To calculate the bubble size distribution $N_{\text{bubble}}(A)$ and bubble fraction f_{bubble} for each system size $[(L_x, L_y) = (100, 50), (200, 100), (400, 200)]$ and solvent activity $\varepsilon_{\text{solvent}}$, which are plotted in Fig. 3, we used configurations of 16 independent samples with 90 time points each, taken every 10^6 MC steps after relaxation with 10^7 MC steps using the separated initial state [Fig. 9(b)]. In Fig. 12, we show the time evolution of f_{bubble} obtained by averaging over 16 independent samples for the largest system size $[(L_x, L_y) = (400, 200)]$ at (a) $\rho = 0.5$ or (b) $\rho = 0.8$.

4. Critical phenomena in symmetric limit

a. Statistical properties of order parameter and related quantities

To obtain the ensemble-averaged quantities (i.e., Binder ratio Q , order parameter ϕ , and susceptibility χ) for each system size $[(L_x, L_y) = (70, 35), (100, 50), (140, 70), (200, 100), (280, 140)]$ and activity ε , which are used in Fig. 8, we took configurations of 400 independent samples with 90 time points each, using the random initial state [Fig. 9(a)]. The samples are taken every 10^5 MC steps after relaxation with 10^6 MC steps for $(L_x, L_y) = (70, 35)$ and $(L_x, L_y) = (100, 50)$; taken every 4×10^5 MC steps after relaxation with 4×10^6 MC steps for $(L_x, L_y) = (140, 70)$ and $(L_x, L_y) = (200, 100)$; and taken every 6×10^5 MC steps after relaxation with 6×10^6 MC steps for $(L_x, L_y) = (280, 140)$. In Fig. 13(a), we plot the time evolution of the order parameter $\hat{\phi}$ averaged over 400 independent samples for the largest system size $[(L_x, L_y) = (280, 140)]$.

We calculated the effective sample size n_{eff} in the following way. The normalized autocorrelation function $C_\phi(t_{\text{lag}})$ is defined as [77]

$$C_\phi(t_{\text{lag}}) := \frac{\langle \delta\hat{\phi}(t) \delta\hat{\phi}(t + t_{\text{lag}}) \rangle}{\langle (\delta\hat{\phi})^2 \rangle}, \quad (\text{A3})$$

where t_{lag} is the time lag, $\delta\hat{\phi}(t) := \hat{\phi}(t) - \langle \hat{\phi} \rangle$ is the order parameter fluctuation for a configuration at time t , and $\langle \dots \rangle$ means the ensemble average in the steady state. Practically, we calculated $C_\phi(t_{\text{lag}})$ by averaging over independent samples and time points after relaxation [see the gray area in Fig. 13(a) for $L_x = 280$]. For $L_x = 70, 100, 140$, we confirmed that C_ϕ is small ($C_\phi < 0.015$) at the time lag between two consecutive observation points; thus, the effective sample size is calculated as $n_{\text{eff}} = n_{\text{sample}} n_{\text{time}}$, where $n_{\text{sample}} = 400$ and $n_{\text{time}} = 90$ are the total numbers of independent samples and observation time points, respectively. On the other hand, for $L_x = 200$ and $L_x = 280$, we found non-negligible autocorrelation as shown in Figs. 13(b) and 13(c), respectively; thus, the effective sample size is calculated as $n_{\text{eff}} = n_{\text{sample}} n_{\text{time}} / [1 + 2 \sum_{1 \leq i \leq 10} C(t_{\text{lag}, i})]$ by taking into account the correction by autocorrelation [77], where $t_{\text{lag}, i}$ is the i th smallest time lag among observation time points. The calculated n_{eff} is plotted in Fig. 13(d), which shows the decrease in the effective sample size for $L_x = 200$ and $L_x = 280$.

The standard error for Q , ϕ , and χ are obtained as follows. First, σ_ϕ (standard deviation for ϕ) is obtained from the configurations used to calculate the mean value ϕ . Then, using the error propagation formula, we obtain σ_Q and σ_χ (standard deviations for Q and χ , respectively). Lastly, using the effective sample size n_{eff} obtained above, we estimate the standard errors as $\sigma_q / \sqrt{n_{\text{eff}}}$ for $q = Q, \phi, \chi$. These standard errors are used for error bars in Figs. 8(a)-8(d).

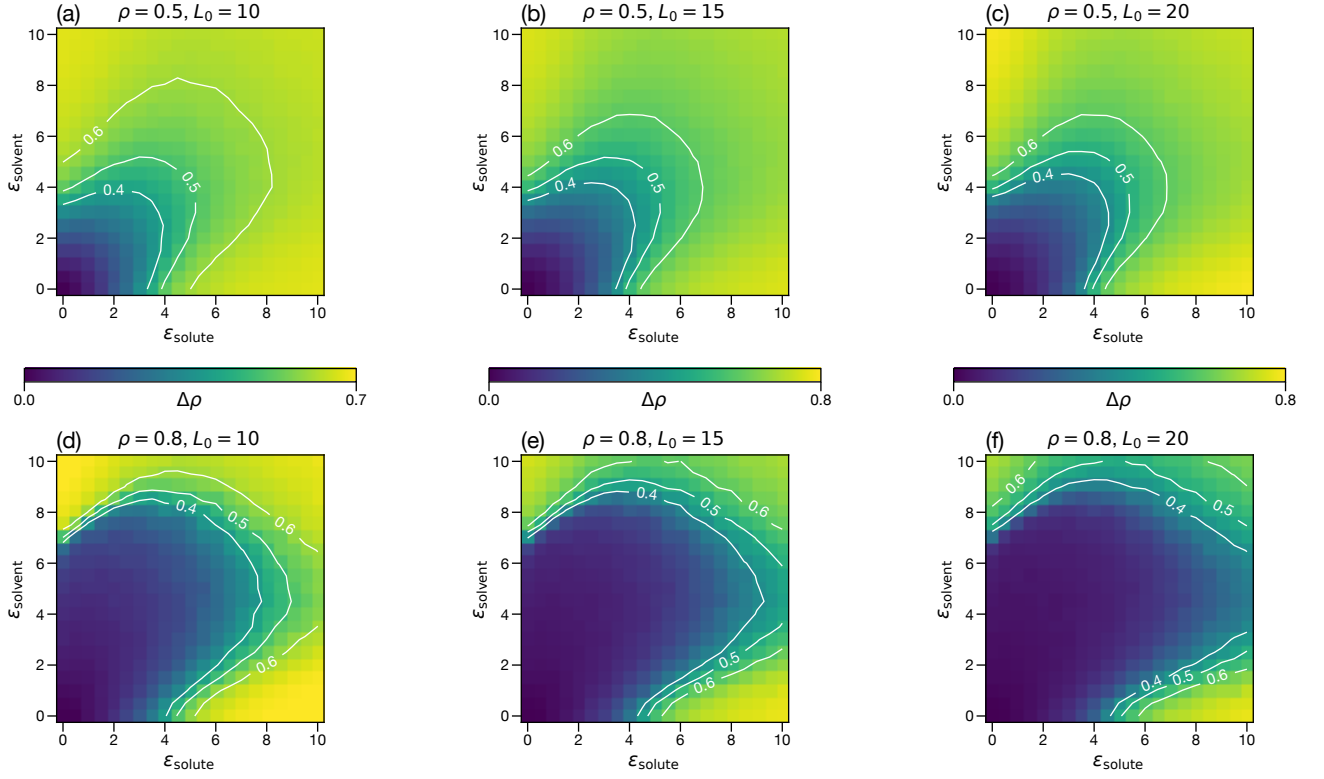


FIG. 11. Weak dependence of the qualitative phase diagram on the definition of $\Delta\rho$. (a-c) Heatmaps and contour lines of the shifted density difference $\Delta\rho$, a degree of phase separation, for $\rho = 0.5$, obtained using subsystems of size $L_0 \times L_0$ with (a) $L_0 = 10$, (b) $L_0 = 15$, and (c) $L_0 = 20$. (d-f) Counterparts for $\rho = 0.8$. For all plots, the used system size is $(L_x, L_y) = (100, 50)$. Panels (a) and (d) correspond to Figs. 2(a) and 2(b), respectively.

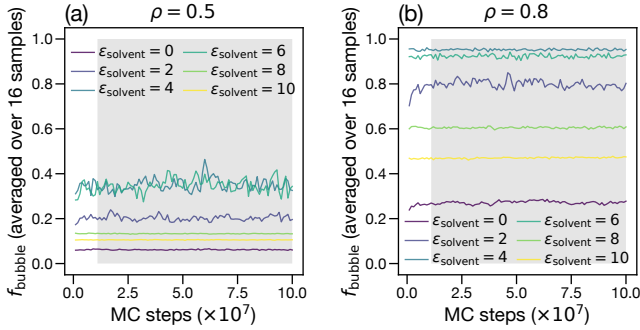


FIG. 12. Time evolution of f_{bubble} . (a, b) Time-dependent f_{bubble} for $(L_x, L_y) = (400, 200)$ and several $\varepsilon_{\text{solvent}}$ at (a) $\rho = 0.5$ or (b) $\rho = 0.8$. In (a) and (b), the gray area indicates the time points used for averaging to produce Figs. 3(a-d) and 3(e-h), respectively.

b. Finite-size scaling analysis

To determine ε_c and ν , we performed nonlinear least squares fitting of the data for $Q(\varepsilon, L_x)$ using a polynomial function that satisfies the scaling hypothesis [Eq. (15)]. The fitting was carried out with a Python package (`scipy.optimize.curve_fit` [69]). Specifically, we used $a_0 + a_1 L_x^{1/\tilde{\nu}}(\varepsilon - \tilde{\varepsilon}_c) + a_2 L_x^{2/\tilde{\nu}}(\varepsilon - \tilde{\varepsilon}_c)^2 + a_3 L_x^{3/\tilde{\nu}}(\varepsilon - \tilde{\varepsilon}_c)^3 + a_4 L_x^{4/\tilde{\nu}}(\varepsilon -$

$\tilde{\varepsilon}_c)^4$ as the fitting function, where $\{a_i\}_{i=0}^4$, $\tilde{\varepsilon}_c$, and $\tilde{\nu}$ are fitting parameters. We used the standard error of Q (see Appendix A 4 a) as uncertainty. In Fig. 14(a), we show the fitted curves for the three largest system sizes ($L_x = 140, 200, 280$). The optimal values, $\tilde{\varepsilon}_c = \varepsilon_c$ and $\tilde{\nu} = \nu$, which are obtained using the data set for three sequential system sizes, are plotted in Figs. 8(e) and 8(f) with black dots, shown with fitting errors $\pm\delta\varepsilon_c$ and $\pm\delta\nu$ suggested by shading, respectively.

For each pair taken from $\{\varepsilon_c, \varepsilon_c + \delta\varepsilon_c, \varepsilon_c - \delta\varepsilon_c\}$ and $\{\nu, \nu + \delta\nu, \nu - \delta\nu\}$, which is used as a representative value of $(\tilde{\varepsilon}_c, \tilde{\nu})$, we performed fitting of the data for $\phi(\varepsilon, L_x)$. Specifically, for each pair $(\tilde{\varepsilon}_c, \tilde{\nu})$ [e.g., $(\tilde{\varepsilon}_c, \tilde{\nu}) = (\varepsilon_c + \delta\varepsilon_c, \nu - \delta\nu)$], we used $L_x^{-\tilde{\beta}'} [b_0 + b_1 L_x^{1/\tilde{\nu}}(\varepsilon - \tilde{\varepsilon}_c) + b_2 L_x^{2/\tilde{\nu}}(\varepsilon - \tilde{\varepsilon}_c)^2 + b_3 L_x^{3/\tilde{\nu}}(\varepsilon - \tilde{\varepsilon}_c)^3 + b_4 L_x^{4/\tilde{\nu}}(\varepsilon - \tilde{\varepsilon}_c)^4]$ as the fitting function, where $\{b_i\}_{i=0}^4$ and $\tilde{\beta}'$ are fitting parameters. We used the standard error of ϕ (see Appendix A 4 a) as uncertainty. In Fig. 14(b), we show the fitted curves for the three largest system sizes ($L_x = 140, 200, 280$) when taking $(\tilde{\varepsilon}_c, \tilde{\nu}) = (\varepsilon_c, \nu)$. We obtained the optimal value, $\tilde{\beta}' = \beta'$ ($= \beta/\nu$), for each pair $(\tilde{\varepsilon}_c, \tilde{\nu})$; we chose β' at $(\tilde{\varepsilon}_c, \tilde{\nu}) = (\varepsilon_c, \nu)$ as the estimated value, which is plotted in Fig. 8(g) with black dots. We also obtained the fitting error $\pm\delta\beta'$ for each pair $(\tilde{\varepsilon}_c, \tilde{\nu})$; the maximum value of $\beta' + \delta\beta'$ over all (i.e., nine) pairs of $(\tilde{\varepsilon}_c, \tilde{\nu})$ was used for the upper estimation error, and the minimum value of $\beta' - \delta\beta'$ was used for the lower estimation error, as plotted in Fig. 8(g) with shading.

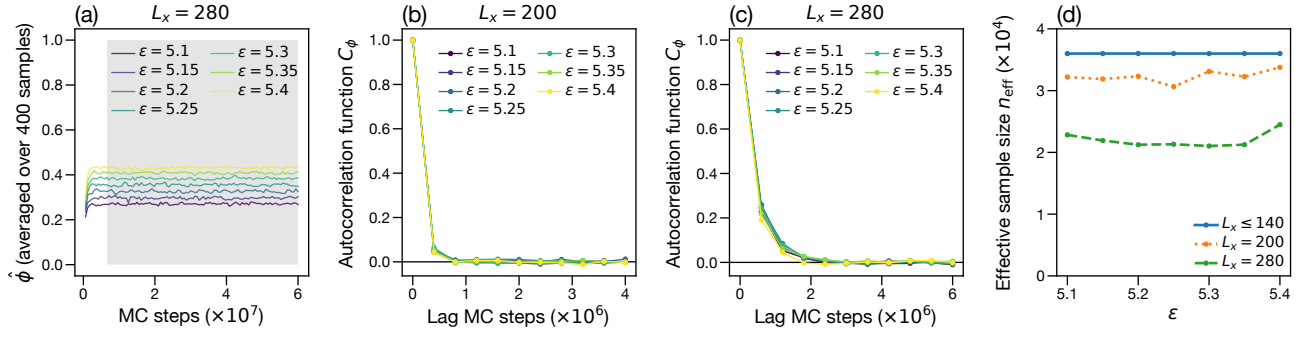


FIG. 13. Statistical properties of order parameter $\hat{\phi}$ at $\rho = 0.5$ in the symmetric limit ($\varepsilon_{\text{solute}} = \varepsilon_{\text{solvent}} = \varepsilon$) for rectangular systems ($L_x/L_y = 2$). (a) Time evolution of $\hat{\phi}$ (averaged over independent samples) for different ε with $L_x = 280$. The gray area indicates the time points used for averaging to produce Fig. 8. (b, c) Autocorrelation function C_ϕ as a function of time lag for different ε and (b) $L_x = 200$ or (c) $L_x = 280$. (d) Effective sample size n_{eff} as a function of ε for $L_x \leq 140$ (blue solid line), $L_x = 200$ (orange dotted line), and $L_x = 280$ (green dashed line).

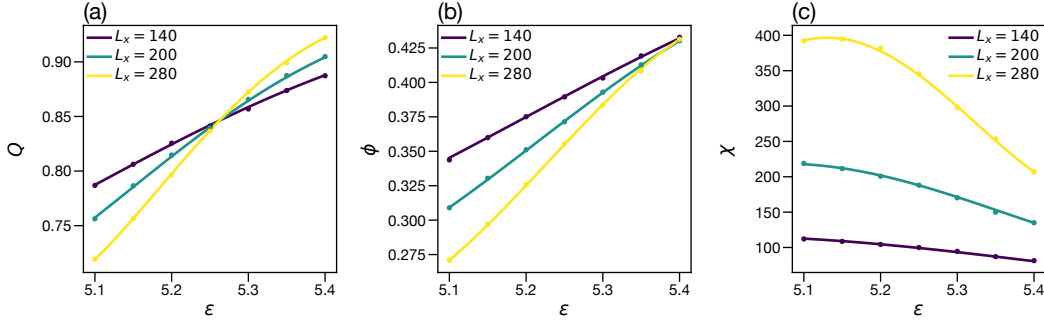


FIG. 14. Fitting physical quantities to polynomial functions under the finite-size scaling hypothesis. (a-c) The fitted curves (colored solid lines) for the three largest system sizes ($L_x = 140, 200, 280$), shown with the observed data (colored dots) of the (a) Binder ratio Q , (b) order parameter ϕ , and (c) susceptibility χ .

We obtained γ' ($= \gamma/\nu$) and its estimation error by fitting the data for $\chi(\varepsilon, L_x)$ in the same way as used for β' ($= \beta/\nu$). Specifically, we used $L_x^{\tilde{\gamma}} [c_0 + c_1 L_x^{1/\tilde{\nu}} (\varepsilon - \tilde{\varepsilon}_c) + c_2 L_x^{2/\tilde{\nu}} (\varepsilon - \tilde{\varepsilon}_c)^2 + c_3 L_x^{3/\tilde{\nu}} (\varepsilon - \tilde{\varepsilon}_c)^3 + c_4 L_x^{4/\tilde{\nu}} (\varepsilon - \tilde{\varepsilon}_c)^4]$ as the fitting function, where $\{c_i\}_{i=0}^4$ and $\tilde{\gamma}$ are fitting parameters, and used the standard error of χ (see Appendix A 4 a) as uncertainty. In Fig. 14(c), we show the fitted curves for the three largest system sizes ($L_x = 140, 200, 280$) when taking $(\tilde{\varepsilon}_c, \tilde{\nu}) = (\varepsilon_c, \nu)$. The estimated γ' and its error are plotted in Fig. 8(h).

c. Validation of fitting procedure for equilibrium lattice gas

To confirm the validity of the fitting procedure explained in Appendix A 4 b for a well-known model, we consider equilibrium lattice gas, where N ($= \rho_{\text{LG}} L_x L_y$) particles are interacting in equilibrium on a rectangular lattice of size (L_x, L_y) with periodic boundary conditions along the x and y axes. We write the equilibrium distribution for this model as $P_{\text{eq}}(\mathbf{n})$, where $\mathbf{n} := \{n_i\}$ is the particle configuration with $n_i \in \{0, 1\}$ indicating the occupancy at site i . We assume $\ln P_{\text{eq}}(\mathbf{n}) = U \sum_{\langle i,j \rangle} n_i n_j + \text{const.}$, where U is the dimensionless attractive interaction strength, and $\sum_{\langle i,j \rangle} (\dots)$ represents the summation over nearest-neighbor sites. It has been known that, in the thermodynamic limit, this model undergoes critical phase sep-

aration at $U = U_c^{\text{exact}} := 2 \ln(1 + \sqrt{2})$ and $\rho_{\text{LG}} = 0.5$ with critical exponents in the two-dimensional Ising universality class [83].

We implement the stochastic dynamics in which the steady-state distribution coincides with $P_{\text{eq}}(\mathbf{n})$ as follows. In a single MC step, we update the configuration as follows:

- (1) We randomly choose a particle and an empty site.
- (2) The chosen particle hops to the chosen empty site with probability $1/[1 + \exp(-U\Delta n)]$, where Δn is the change in the total number of particles adjacent to the chosen particle as a result of the hop.
- (3) We repeat procedures (1) and (2) N times.

We stress that we allow not only the nearest-neighbor hopping, which is used in the Kawasaki dynamics, but also any nonlocal hopping, which accelerates the convergence to the steady state [77, 84–87]. Note that the nonequilibrium extension of similar models with nonlocal hopping has been numerically found to undergo critical phase separation with the Ising critical exponents [59].

To apply the finite-size scaling analysis, we consider different system sizes ($L_x = 26, 36, 50, 70, 100, 140$) with fixed $L_x/L_y = 2$ and several values of U near U_c^{exact} at $\rho_{\text{LG}} = 0.5$.

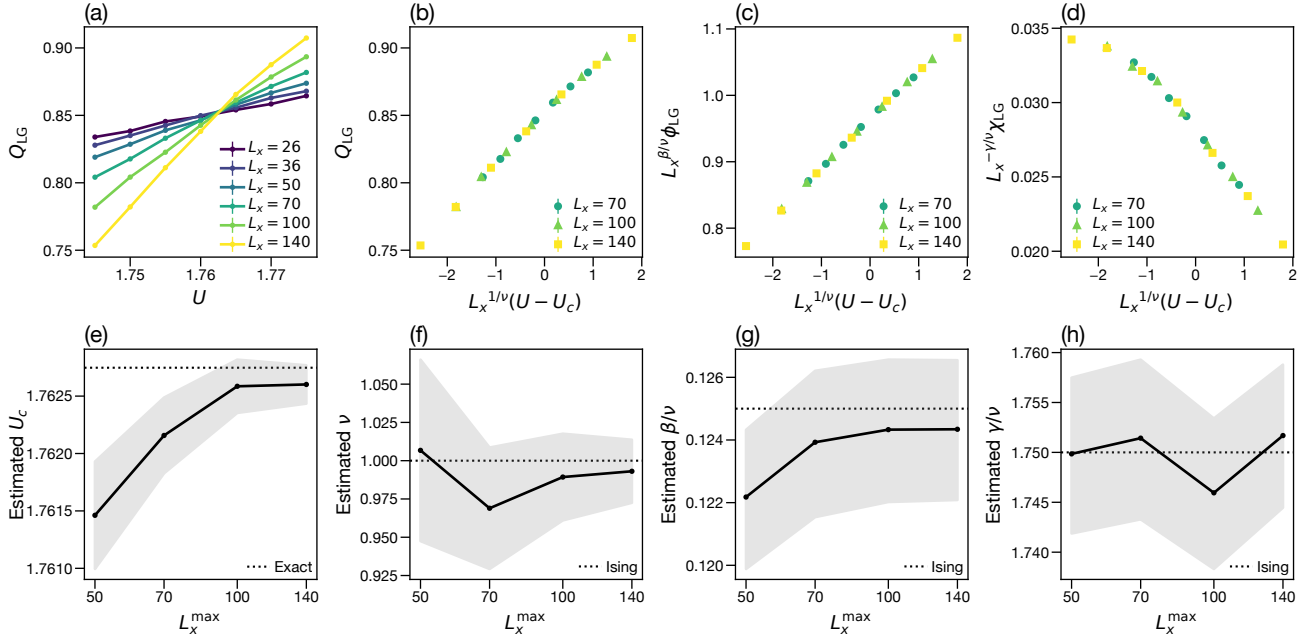


FIG. 15. Ising universality for critical phenomena in the equilibrium lattice gas model. (a) Binder ratio Q_{LG} as a function of interaction strength U for different system sizes with fixed $L_x/L_y = 2$. (b-d) Rescaled plots of the (b) Binder ratio Q_{LG} , (c) order parameter ϕ_{LG} , and (d) susceptibility χ_{LG} , based on the finite-size scaling hypothesis for the three largest system sizes. (e) Estimated critical point U_c as a function of L_x^{\max} , the maximum L_x in the data set used for fitting, where the dotted line suggests the exact critical point $U_c^{\text{exact}} = 2 \ln(1 + \sqrt{2})$ [83]. (f-h) Estimated critical exponents (ν , β/ν , and γ/ν) as a function of L_x^{\max} , where the dotted lines suggest the Ising critical exponents. In (e-h), the estimation error is indicated by shading.

We define the order parameter $\hat{\phi}_{LG}$ in the same way as used in Eq. (14):

$$\hat{\phi}_{LG} := \frac{\sin(\pi/L_x)}{L_y} \left| \sum_j e^{-2\pi i j_x / L_x} n_j \right|. \quad (\text{A4})$$

To obtain the Binder ratio $Q_{LG} := \langle \hat{\phi}_{LG}^2 \rangle^2 / \langle \hat{\phi}_{LG} \rangle^4$, (ensemble-averaged) order parameter $\phi_{LG} := \langle \hat{\phi}_{LG} \rangle$, and susceptibility $\chi_{LG} := L_x L_y (\langle \hat{\phi}_{LG}^2 \rangle - \langle \hat{\phi}_{LG} \rangle^2)$, we took configurations of 1000 independent samples with 90 time points each, using the initial state with a random distribution of particles. The samples are taken every 10^3 MC steps after relaxation with 10^4 MC steps for $L_x = 26$ and $L_x = 36$; taken every 10^4 MC steps after relaxation with 10^5 MC steps for $L_x = 50$, $L_x = 70$, and $L_x = 100$; and taken every 5×10^4 MC steps after relaxation with 5×10^5 MC steps for $L_x = 140$. We confirmed that normalized autocorrelation function for $\hat{\phi}_{LG}$ is small (< 0.01) at the time lag between two consecutive observation points for all L_x and U ; thus, the effective sample size is calculated as $n_{\text{eff}} = 1000 \times 90 = 9 \times 10^4$ for each L_x and U .

In the same way as used in Appendix A 4 b, we performed fitting of the obtained data based on the finite-size scaling hypothesis. The results are shown in Fig. 15. First, Fig. 15(a) shows approximate crossing of the Binder ratio Q_{LG} , suggesting the value of the critical point U_c . In Fig. 15(e), we plot the estimated U_c (black dots) as a function of L_x^{\max} , the maximum L_x in the used data set with three sequential system sizes (e.g., $L_x^{\max} = 100$ for $L_x \in \{50, 70, 100\}$). This

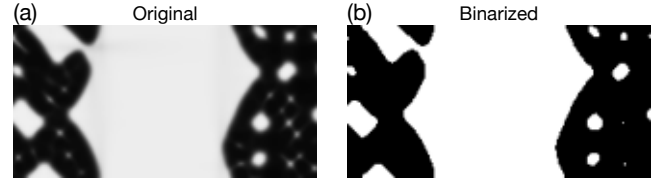


FIG. 16. Binarized solute density in mean-field dynamics. (a, b) Example of snapshots for (a) the original solute density $\rho_{i,\text{solute}}$ and (b) the binarized counterpart. The used parameters are $(L_x, L_y) = (200, 100)$, $\rho = 0.5$, and $(\varepsilon_{\text{solute}}, \varepsilon_{\text{solvent}}) = (10, 3)$.

suggests that the fitting procedure works well to obtain U_c close to U_c^{exact} (dotted line). Then, we present the estimated critical exponents (ν , β/ν , and γ/ν) as a function of L_x in Figs. 15(f)-15(h) with black dots, showing that the estimated values are close to the Ising exponents (dotted lines), as expected from theory [83]. Each of the rescaled plots shown in Figs. 15(b)-15(d) suggests the universal scaling form independent of L_x , consistent with the finite-size scaling hypothesis. Quantitatively, for the data set with the largest L_x^{\max} , the fitting procedure resulted in $U_c = 1.7626(2)$, $\nu = 0.99(2)$, $\beta/\nu = 0.124(2)$, and $\gamma/\nu = 1.752(7)$, which are close to the exact values, $U_c^{\text{exact}} = 1.7627\dots$, $\nu_{\text{Ising}} = 1$, $\beta_{\text{Ising}}/\nu_{\text{Ising}} = 0.125$, and $\gamma_{\text{Ising}}/\nu_{\text{Ising}} = 1.75$, respectively.

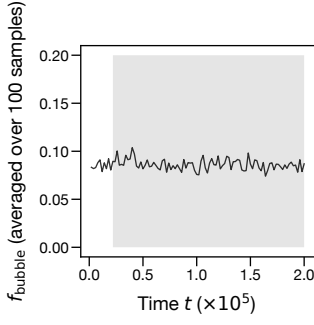


FIG. 17. Time evolution of f_{bubble} in mean-field dynamics. The used parameters are $(L_x, L_y) = (200, 100)$, $\rho = 0.5$, and $(\varepsilon_{\text{solute}}, \varepsilon_{\text{solvent}}) = (10, 3)$. The gray area indicates the time points used for averaging to produce Figs. 6(d) and 6(e).

Appendix B: Mean-field theory

1. Bubble formation in mean-field dynamics

We specify the solvent bubbles for the mean-field dynamics as follows. First, we binarize the local solute density $\rho_{i,\text{solute}}$ with a threshold value 0.5 (see Fig. 16 for an example). Then, in the same way as used for the stochastic dynamics (see Appendix A 3), we define the bubbles as clusters of solvents, excluding the largest cluster, which is regarded as the bulk solvent-rich phase.

To calculate the bubble size distribution $N_{\text{bubble}}(A)$ and bubble fraction f_{bubble} at $\rho = 0.5$ and $(\varepsilon_{\text{solute}}, \varepsilon_{\text{solvent}}) = (10, 3)$ for each system size $[(L_x, L_y) = (100, 50), (140, 70), (200, 100)]$, which are plotted in Figs. 6(d) and 6(e), we used configurations of 100 independent samples with 90 time points each, taken every 10^5 steps with time step $dt = 0.02$ after relaxation with 10^6 steps using the separated initial state [Fig. 9(b)]. In Fig. 17, we show the time evolution of f_{bubble} obtained by averaging over 100 independent samples for the largest system size $[(L_x, L_y) = (200, 100)]$.

2. Linear stability analysis for single-site mean-field theory

The explicit form of Eq. (4) is given as

$$\begin{aligned} \partial_t \rho_{i,s,p} = & \sum_{l \in \{\pm \bar{s}, \pm \bar{y}\}} \sum_{p'} (\rho_{i,\bar{s},p'} \rho_{i+l,s,p} - \rho_{i+l,\bar{s},p'} \rho_{i,s,p}) + \sum_{p'} \varepsilon_s (\rho_{i,\bar{s},p'} \rho_{i-p,s,p} - \rho_{i+p,\bar{s},p'} \rho_{i,s,p}) + \sum_{p'} \varepsilon_{\bar{s}} (\rho_{i,\bar{s},p'} \rho_{i+p',s,p} - \rho_{i-p',\bar{s},p'} \rho_{i,s,p}) \\ & + \gamma (\rho_{i,s,Rp} + \rho_{i,s,R^{-1}p} - 2\rho_{i,s,p}). \end{aligned} \quad (\text{B1})$$

We linearize this equation in terms of the local fluctuations around the homogeneous state [i.e., $\rho_{i,\text{solute},p} = \rho/4$ and $\rho_{i,\text{solvent},p} = (1 - \rho)/4$ for any i or p]. Using $\rho_{k,s,p} = \sum_j e^{-ik \cdot j} \rho_{j,s,p}$, we obtain

$$\begin{aligned} \partial_t \rho_{k,s,p} = & -\frac{1}{4} \sum_{p'} 2(2 - \cos k_x - \cos k_y) (\rho_{\bar{s}} \rho_{k,s,p} - \rho_s \rho_{k,\bar{s},p'}) - \frac{1}{4} \sum_{p'} \varepsilon_s [(1 - e^{-ik \cdot p}) \rho_{\bar{s}} \rho_{k,s,p} - (1 - e^{ik \cdot p}) \rho_s \rho_{k,\bar{s},p'}] \\ & - \frac{1}{4} \sum_{p'} \varepsilon_{\bar{s}} [(1 - e^{ik \cdot p'}) \rho_{\bar{s}} \rho_{k,s,p} - (1 - e^{-ik \cdot p'}) \rho_s \rho_{k,\bar{s},p'}] - \gamma (2\rho_{k,s,p} - \rho_{k,s,Rp} - \rho_{k,s,R^{-1}p}) \\ = & -2(2 - \cos k_x - \cos k_y) \left[\rho_{\bar{s}} \rho_{k,s,p} - \frac{1}{4} \rho_s \sum_{p'} \rho_{k,\bar{s},p'} \right] - \varepsilon_s \left[(1 - e^{-ik \cdot p}) \rho_{\bar{s}} \rho_{k,s,p} - \frac{1}{4} (1 - e^{ik \cdot p}) \rho_s \sum_{p'} \rho_{k,\bar{s},p'} \right] \\ & - \varepsilon_{\bar{s}} \left[\frac{1}{2} (2 - \cos k_x - \cos k_y) \rho_{\bar{s}} \rho_{k,s,p} - \frac{1}{4} \rho_s \sum_{p'} (1 - e^{-ik \cdot p'}) \rho_{k,\bar{s},p'} \right] - \gamma (2\rho_{k,s,p} - \rho_{k,s,Rp} - \rho_{k,s,R^{-1}p}), \end{aligned} \quad (\text{B2})$$

where $\rho_{\text{solute}} := \rho$, $\rho_{\text{solvent}} := 1 - \rho$, and \bar{s} represents the species opposite to s . Considering $\rho_{k,s,p}$ as a component of 8-dimensional vector $\boldsymbol{\rho}_k$, we can write Eq. (B2) in the form of $\partial_t \boldsymbol{\rho}_k = R_k^{\text{MF1}} \boldsymbol{\rho}_k$ with 8×8 matrix R_k^{MF1} .

To examine linear stability against small-wavenumber fluctuations, we expand the coefficients in Eq. (B2) in terms of \boldsymbol{k} up to

$O(|\mathbf{k}|^4)$:

$$\begin{aligned} \partial_t \rho_{k,s,p} = & - \left(|\mathbf{k}|^2 - \frac{1}{12} k_x^4 - \frac{1}{12} k_y^4 \right) \left[\rho_{\bar{s}} \rho_{k,s,p} - \frac{1}{4} \rho_s \sum_{p'} \rho_{k,\bar{s},p'} \right] - \varepsilon_s \left[i \mathbf{k} \cdot \mathbf{p} + \frac{1}{2} (\mathbf{k} \cdot \mathbf{p})^2 - \frac{i}{6} (\mathbf{k} \cdot \mathbf{p})^3 - \frac{1}{24} (\mathbf{k} \cdot \mathbf{p})^4 \right] \rho_{\bar{s}} \rho_{k,s,p} \\ & - \frac{1}{4} \varepsilon_s \left[i \mathbf{k} \cdot \mathbf{p} - \frac{1}{2} (\mathbf{k} \cdot \mathbf{p})^2 - \frac{i}{6} (\mathbf{k} \cdot \mathbf{p})^3 + \frac{1}{24} (\mathbf{k} \cdot \mathbf{p})^4 \right] \rho_s \sum_{p'} \rho_{k,\bar{s},p'} - \frac{1}{4} \varepsilon_{\bar{s}} \left(|\mathbf{k}|^2 - \frac{1}{12} k_x^4 - \frac{1}{12} k_y^4 \right) \rho_{\bar{s}} \rho_{k,s,p} \\ & + \frac{1}{4} \varepsilon_{\bar{s}} \rho_s \sum_{p'} \left[i \mathbf{k} \cdot \mathbf{p}' + \frac{1}{2} (\mathbf{k} \cdot \mathbf{p}')^2 - \frac{i}{6} (\mathbf{k} \cdot \mathbf{p}')^3 - \frac{1}{24} (\mathbf{k} \cdot \mathbf{p}')^4 \right] \rho_{k,\bar{s},p'} - \gamma (2\rho_{k,s,p} - \rho_{k,s,Rp} - \rho_{k,s,R^{-1}p}). \end{aligned} \quad (\text{B3})$$

We introduce the density fluctuation $\rho_{k,s} := \sum_p \rho_{k,s,p}$, polarity density fluctuation $\mathbf{w}_{k,s} := \sum_p p \rho_{k,s,p}$, and nematicity density fluctuation $\nu_{k,s} := \sum_p (p_x^2 - p_y^2) \rho_{k,s,p}$. Noticing that $\rho_{k,\bar{s}} = -\rho_{k,s}$ and $\rho_{\bar{s}} = 1 - \rho_s$, we rewrite Eq. (B3) as

$$\begin{aligned} \partial_t \rho_{k,s} = & - \left(1 + \frac{1}{4} \varepsilon_s + \frac{1}{4} \varepsilon_{\bar{s}} \right) \left(|\mathbf{k}|^2 - \frac{1}{12} k_x^4 - \frac{1}{12} k_y^4 \right) \rho_{k,s} - i \varepsilon_s (1 - \rho_s) \left(\mathbf{k} \cdot \mathbf{w}_{k,s} - \frac{1}{6} k_x^3 w_{x,k,s} - \frac{1}{6} k_y^3 w_{y,k,s} \right) \\ & + i \varepsilon_{\bar{s}} \rho_s \left(\mathbf{k} \cdot \mathbf{w}_{k,\bar{s}} - \frac{1}{6} k_x^3 w_{x,k,\bar{s}} - \frac{1}{6} k_y^3 w_{y,k,\bar{s}} \right) - \frac{1}{4} \varepsilon_s (1 - \rho_s) \left(k_x^2 - k_y^2 - \frac{1}{12} k_x^4 + \frac{1}{12} k_y^4 \right) \nu_{k,s} \\ & + \frac{1}{4} \varepsilon_{\bar{s}} \rho_s \left(k_x^2 - k_y^2 - \frac{1}{12} k_x^4 + \frac{1}{12} k_y^4 \right) \nu_{k,\bar{s}}, \end{aligned} \quad (\text{B4})$$

$$\begin{aligned} \partial_t w_{x,k,s} = & -(1 - \rho_s) \left(|\mathbf{k}|^2 - \frac{1}{12} k_x^4 - \frac{1}{12} k_y^4 \right) w_{x,k,s} - \frac{1}{2} \varepsilon_s (1 - \rho_s) \left[i k_x (\rho_{k,s} + \nu_{k,s}) + k_x^2 w_{x,k,s} - \frac{i}{6} k_x^3 (\rho_{k,s} + \nu_{k,s}) - \frac{1}{12} k_x^4 w_{x,k,s} \right] \\ & + \frac{1}{2} \varepsilon_s \rho_s \left(i k_x - \frac{i}{6} k_x^3 \right) \rho_{k,s} - \frac{1}{4} \varepsilon_{\bar{s}} (1 - \rho_s) \left(|\mathbf{k}|^2 - \frac{1}{12} k_x^4 - \frac{1}{12} k_y^4 \right) w_{x,k,s} - 2\gamma w_{x,k,s}, \end{aligned} \quad (\text{B5})$$

$$\begin{aligned} \partial_t w_{y,k,s} = & -(1 - \rho_s) \left(|\mathbf{k}|^2 - \frac{1}{12} k_x^4 - \frac{1}{12} k_y^4 \right) w_{y,k,s} - \frac{1}{2} \varepsilon_s (1 - \rho_s) \left[i k_y (\rho_{k,s} - \nu_{k,s}) + k_y^2 w_{y,k,s} - \frac{i}{6} k_y^3 (\rho_{k,s} - \nu_{k,s}) - \frac{1}{12} k_y^4 w_{y,k,s} \right] \\ & + \frac{1}{2} \varepsilon_s \rho_s \left(i k_y - \frac{i}{6} k_y^3 \right) \rho_{k,s} - \frac{1}{4} \varepsilon_{\bar{s}} (1 - \rho_s) \left(|\mathbf{k}|^2 - \frac{1}{12} k_x^4 - \frac{1}{12} k_y^4 \right) w_{y,k,s} - 2\gamma w_{y,k,s}, \end{aligned} \quad (\text{B6})$$

$$\begin{aligned} \partial_t \nu_{k,s} = & -(1 - \rho_s) \left(|\mathbf{k}|^2 - \frac{1}{12} k_x^4 - \frac{1}{12} k_y^4 \right) \nu_{k,s} - \varepsilon_s (1 - \rho_s) \left[i k_x w_{x,k,s} - i k_y w_{y,k,s} + \frac{1}{4} k_x^2 (\rho_{k,s} + \nu_{k,s}) - \frac{1}{4} k_y^2 (\rho_{k,s} - \nu_{k,s}) \right] \\ & - \varepsilon_s (1 - \rho_s) \left[-\frac{i}{6} k_x^3 w_{x,k,s} + \frac{i}{6} k_y^3 w_{y,k,s} - \frac{1}{48} k_x^4 (\rho_{k,s} + \nu_{k,s}) + \frac{1}{48} k_y^4 (\rho_{k,s} - \nu_{k,s}) \right]. \end{aligned} \quad (\text{B7})$$

To find the linear instability condition for $\mathbf{k} \rightarrow \mathbf{0}$, which corresponds to macroscopic phase separation, we apply the adiabatic approximation [71, 72] to the equations for fast variables $\mathbf{w}_{k,s}$ [Eqs. (B5) and (B6)] and $\nu_{k,s}$ [Eq. (B7)], which leads to

$$\begin{aligned} w_{x,k,s} = & \frac{i}{4\gamma} \varepsilon_s (2\rho_s - 1) \left(k_x - \frac{1}{6} k_x^3 \right) \rho_{k,s} - \frac{i}{8\gamma^2} \varepsilon_s \left(1 + \frac{1}{4} \varepsilon_{\bar{s}} \right) (1 - \rho_s) (2\rho_s - 1) k_x |\mathbf{k}|^2 \rho_{k,s} \\ & - \frac{i}{16\gamma^2} \varepsilon_s^2 (1 - \rho_s) (2\rho_s - 1) k_x^3 \rho_{k,s} - \frac{i}{4\gamma} \varepsilon_s (1 - \rho_s) k_x \nu_{k,s} + O(|\mathbf{k}|^5 \rho_{k,s}, |\mathbf{k}|^3 \nu_{k,s}), \end{aligned} \quad (\text{B8})$$

$$\begin{aligned} w_{y,k,s} = & \frac{i}{4\gamma} \varepsilon_s (2\rho_s - 1) \left(k_y - \frac{1}{6} k_y^3 \right) \rho_{k,s} - \frac{i}{8\gamma^2} \varepsilon_s \left(1 + \frac{1}{4} \varepsilon_{\bar{s}} \right) (1 - \rho_s) (2\rho_s - 1) k_y |\mathbf{k}|^2 \rho_{k,s} \\ & - \frac{i}{16\gamma^2} \varepsilon_s^2 (1 - \rho_s) (2\rho_s - 1) k_y^3 \rho_{k,s} + \frac{i}{4\gamma} \varepsilon_s (1 - \rho_s) k_y \nu_{k,s} + O(|\mathbf{k}|^5 \rho_{k,s}, |\mathbf{k}|^3 \nu_{k,s}), \end{aligned} \quad (\text{B9})$$

$$\nu_{k,s} = -\frac{1}{16\gamma} \varepsilon_s (k_x^2 - k_y^2) \rho_{k,s} - \frac{i}{4\gamma} \varepsilon_s (1 - \rho_s) (k_x w_{x,k,s} - k_y w_{y,k,s}) + O(|\mathbf{k}|^4 \rho_{k,s}, |\mathbf{k}|^2 \mathbf{k} \cdot \mathbf{w}_{k,s}). \quad (\text{B10})$$

By substituting these into Eq. (B4), we obtain

$$\partial_t \rho_{k,\text{solute}} = r_{\mathbf{k}}^{\text{MF1}} \rho_{k,\text{solute}} \quad (\text{B11})$$

with

$$r_{\mathbf{k}}^{\text{MF1}} = c_2^{\text{MF1}} |\mathbf{k}|^2 + c_{4+}^{\text{MF1}} |\mathbf{k}|^4 + c_{4-}^{\text{MF1}} (k_x^2 - k_y^2)^2 + O(|\mathbf{k}|^6). \quad (\text{B12})$$

Here, the coefficients are

$$c_2^{\text{MF1}} = -\left(1 + \frac{\varepsilon_{\text{solute}} + \varepsilon_{\text{solvent}}}{4}\right) + \frac{\varepsilon_{\text{solute}}^2(1-\rho)(2\rho-1)}{4\gamma} - \frac{\varepsilon_{\text{solvent}}^2\rho(2\rho-1)}{4\gamma}, \quad (\text{B13})$$

$$c_{4+}^{\text{MF1}} = \frac{1}{24}\left(1 + \frac{\varepsilon_{\text{solute}} + \varepsilon_{\text{solvent}}}{4}\right) - \frac{\varepsilon_{\text{solute}}^2(1-\rho)(2\rho-1)}{24\gamma} + \frac{\varepsilon_{\text{solvent}}^2\rho(2\rho-1)}{24\gamma} - \frac{\varepsilon_{\text{solute}}^2}{8\gamma^2}\left(1 + \frac{\varepsilon_{\text{solute}} + \varepsilon_{\text{solvent}}}{4}\right)(1-\rho)^2(2\rho-1) + \frac{\varepsilon_{\text{solvent}}^2}{8\gamma^2}\left(1 + \frac{\varepsilon_{\text{solute}} + \varepsilon_{\text{solvent}}}{4}\right)\rho^2(2\rho-1), \quad (\text{B14})$$

$$c_{4-}^{\text{MF1}} = \frac{1}{24}\left(1 + \frac{\varepsilon_{\text{solute}} + \varepsilon_{\text{solvent}}}{4}\right) - \frac{\varepsilon_{\text{solute}}^2(1-\rho)(16\rho-11)}{192\gamma} + \frac{\varepsilon_{\text{solvent}}^2\rho(16\rho-5)}{192\gamma} - \frac{\varepsilon_{\text{solute}}^3(1-\rho)^2(3\rho-2)}{32\gamma^2} + \frac{\varepsilon_{\text{solvent}}^3\rho^2(3\rho-1)}{32\gamma^2} - \frac{\varepsilon_{\text{solute}}^4(1-\rho)^3(2\rho-1)}{64\gamma^3} + \frac{\varepsilon_{\text{solvent}}^4\rho^3(2\rho-1)}{64\gamma^3}. \quad (\text{B15})$$

We numerically confirmed that $c_{4-}^{\text{MF1}} < 0$ near the Lifshitz point, which is determined by $c_2^{\text{MF1}} = 0$ and $c_{4+}^{\text{MF1}} = 0$. This means that, near the Lifshitz point, the diagonal modes (i.e., $k_x = \pm k_y$) are most unstable, compared with other fluctuation modes with the same wavenumber $|\mathbf{k}|$.

3. Explicit form of dynamical equation in four-site mean-field theory

We consider the mean-field dynamical equation for the four-site density $\lambda_{i,\underline{s},\underline{p}}(t)$, where $\underline{s} = (s_1, s_2, s_3, s_4)$ and $\underline{p} = (p_1, p_2, p_3, p_4)$ represent the configuration for a square cluster i , which consists of four sites: $i_1 = i$, $i_2 = i + \hat{x}$, $i_3 = i + \hat{x} + \hat{y}$, and $i_4 = i + \hat{y}$. Neglecting the correlations across square clusters [Fig. 7(b)], we obtain Eq. (12):

$$\partial_t \lambda_{i,\underline{s},\underline{p}} = g_{i,\underline{s},\underline{p}}^{(p,w)} + g_{i,\underline{s},\underline{p}}^{(a,w)} + g_{i,\underline{s},\underline{p}}^{(p,n)} + g_{i,\underline{s},\underline{p}}^{(a,n)} + g_{i,\underline{s},\underline{p}}^{(r)}. \quad (\text{B16})$$

The first term, $g_{i,\underline{s},\underline{p}}^{(p,w)}$, is the contribution from the passive exchange within cluster i . We can divide $g_{i,\underline{s},\underline{p}}^{(p,w)}$ into four terms:

$$g_{i,\underline{s},\underline{p}}^{(p,w)} = g_{i,\underline{s},\underline{p}}^{(p,w,12)} + g_{i,\underline{s},\underline{p}}^{(p,w,23)} + g_{i,\underline{s},\underline{p}}^{(p,w,34)} + g_{i,\underline{s},\underline{p}}^{(p,w,41)}, \quad (\text{B17})$$

where superscript b in $g_{i,\underline{s},\underline{p}}^{(p,w,b)}$ suggests the bond at which the passive exchange occurs (e.g., $g_{i,\underline{s},\underline{p}}^{(p,w,23)}$ corresponds to the exchange of a particle at site $i_2 = i + \hat{x}$ and a particle at site $i_3 = i + \hat{x} + \hat{y}$). Specifically,

$$g_{i,\underline{s},\underline{p}}^{(p,w,12)} = \delta_{s_1, \bar{s}_2} (\lambda_{i,\underline{s}^{12}, \underline{p}^{12}} - \lambda_{i,\underline{s}, \underline{p}}) \quad (\text{B18})$$

$$g_{i,\underline{s},\underline{p}}^{(p,w,23)} = \delta_{s_2, \bar{s}_3} (\lambda_{i,\underline{s}^{23}, \underline{p}^{23}} - \lambda_{i,\underline{s}, \underline{p}}) \quad (\text{B19})$$

$$g_{i,\underline{s},\underline{p}}^{(p,w,34)} = \delta_{s_3, \bar{s}_4} (\lambda_{i,\underline{s}^{34}, \underline{p}^{34}} - \lambda_{i,\underline{s}, \underline{p}}) \quad (\text{B20})$$

$$g_{i,\underline{s},\underline{p}}^{(p,w,41)} = \delta_{s_4, \bar{s}_1} (\lambda_{i,\underline{s}^{41}, \underline{p}^{41}} - \lambda_{i,\underline{s}, \underline{p}}), \quad (\text{B21})$$

where \bar{s} represents the species opposite to s (e.g., solute = solvent), and superscript b in \underline{s}^b or \underline{p}^b suggests the interchanged indices [e.g., $\underline{s}^{23} = (s_1, s_3, s_2, s_4)$]. The first and second terms in each of Eqs. (B18)-(B21) represent the gain and loss of state $(\underline{s}, \underline{p})$ at (i_1, i_2, i_3, i_4) , respectively. Note that Eqs. (B18)-(B21) are derived from the master equation with no approximation.

Similarly, $g_{i,\underline{s},\underline{p}}^{(a,w)}$ is the contribution from the active exchange within cluster i , which is divided into four terms:

$$g_{i,\underline{s},\underline{p}}^{(a,w)} = g_{i,\underline{s},\underline{p}}^{(a,w,12)} + g_{i,\underline{s},\underline{p}}^{(a,w,23)} + g_{i,\underline{s},\underline{p}}^{(a,w,34)} + g_{i,\underline{s},\underline{p}}^{(a,w,41)}. \quad (\text{B22})$$

Specifically,

$$g_{i,\underline{s},\underline{p}}^{(a,w,12)} = \delta_{s_1, \bar{s}_2} [(\varepsilon_{s_1} \delta_{p_1, -\hat{x}} + \varepsilon_{s_2} \delta_{p_2, +\hat{x}}) \lambda_{i,\underline{s}^{12}, \underline{p}^{12}} - (\varepsilon_{s_1} \delta_{p_1, +\hat{x}} + \varepsilon_{s_2} \delta_{p_2, -\hat{x}}) \lambda_{i,\underline{s}, \underline{p}}] \quad (\text{B23})$$

$$g_{i,\underline{s},\underline{p}}^{(a,w,23)} = \delta_{s_2, \bar{s}_3} [(\varepsilon_{s_2} \delta_{p_2, -\hat{y}} + \varepsilon_{s_3} \delta_{p_3, +\hat{y}}) \lambda_{i,\underline{s}^{23}, \underline{p}^{23}} - (\varepsilon_{s_2} \delta_{p_2, +\hat{y}} + \varepsilon_{s_3} \delta_{p_3, -\hat{y}}) \lambda_{i,\underline{s}, \underline{p}}] \quad (\text{B24})$$

$$g_{i,\underline{s},\underline{p}}^{(a,w,34)} = \delta_{s_3, \bar{s}_4} [(\varepsilon_{s_3} \delta_{p_3, +\hat{x}} + \varepsilon_{s_4} \delta_{p_4, -\hat{x}}) \lambda_{i,\underline{s}^{34}, \underline{p}^{34}} - (\varepsilon_{s_3} \delta_{p_3, -\hat{x}} + \varepsilon_{s_4} \delta_{p_4, +\hat{x}}) \lambda_{i,\underline{s}, \underline{p}}] \quad (\text{B25})$$

$$g_{i,\underline{s},\underline{p}}^{(a,w,41)} = \delta_{s_4, \bar{s}_1} [(\varepsilon_{s_4} \delta_{p_4, +\hat{y}} + \varepsilon_{s_1} \delta_{p_1, -\hat{y}}) \lambda_{i,\underline{s}^{41}, \underline{p}^{41}} - (\varepsilon_{s_4} \delta_{p_4, -\hat{y}} + \varepsilon_{s_1} \delta_{p_1, +\hat{y}}) \lambda_{i,\underline{s}, \underline{p}}] \quad (\text{B26})$$

Note that Eqs. (B23)-(B26) are derived from the master equation with no approximation in a similar way as Eqs. (B18)-(B21).

Next, $g_{i,\underline{s},\underline{p}}^{(p,n)}$ corresponds to the passive exchange across cluster i and neighboring clusters. We can divide $g_{i,\underline{s},\underline{p}}^{(p,n)}$ into eight terms:

$$g_{i,\underline{s},\underline{p}}^{(p,n)} = g_{i,\underline{s},\underline{p}}^{(p,n,14')} + g_{i,\underline{s},\underline{p}}^{(p,n,23')} + g_{i,\underline{s},\underline{p}}^{(p,n,21')} + g_{i,\underline{s},\underline{p}}^{(p,n,34')} + g_{i,\underline{s},\underline{p}}^{(p,n,32')} + g_{i,\underline{s},\underline{p}}^{(p,n,41')} + g_{i,\underline{s},\underline{p}}^{(p,n,43')} + g_{i,\underline{s},\underline{p}}^{(p,n,12')}, \quad (\text{B27})$$

where superscript b in $g_{i,\underline{s},\underline{p}}^{(p,n,b)}$ suggests the bond at which the passive exchange occurs, and $(')$ suggests the site index within the neighboring cluster (e.g., $g_{i,\underline{s},\underline{p}}^{(p,n,14')}$ corresponds to the exchange of a particle at site $i_1 = i$ and a particle at site $i_4 - 2\hat{y} = i - \hat{y}$, and $g_{i,\underline{s},\underline{p}}^{(p,n,21')}$ corresponds to the exchange of a particle at site $i_2 = i + \hat{x}$ and a particle at site $i_1 + 2\hat{x} = i + 2\hat{x}$). Specifically,

$$g_{i,\underline{s},\underline{p}}^{(p,n,14')} = \sum_{\underline{s}',\underline{p}'} \delta_{s_1,\bar{s}'_4} (\lambda_{i,\underline{s}^1 \rightarrow 4', \underline{p}^1 \rightarrow 4'} \lambda_{i-2\hat{y},\underline{s}'^{4'} \rightarrow 1, \underline{p}'^{4'} \rightarrow 1} - \lambda_{i,\underline{s},\underline{p}} \lambda_{i-2\hat{y},\underline{s}',\underline{p}'}) \quad (\text{B28})$$

$$g_{i,\underline{s},\underline{p}}^{(p,n,23')} = \sum_{\underline{s}',\underline{p}'} \delta_{s_2,\bar{s}'_3} (\lambda_{i,\underline{s}^2 \rightarrow 3', \underline{p}^2 \rightarrow 3'} \lambda_{i-2\hat{y},\underline{s}'^{3'} \rightarrow 2, \underline{p}'^{3'} \rightarrow 2} - \lambda_{i,\underline{s},\underline{p}} \lambda_{i-2\hat{y},\underline{s}',\underline{p}'}) \quad (\text{B29})$$

$$g_{i,\underline{s},\underline{p}}^{(p,n,21')} = \sum_{\underline{s}',\underline{p}'} \delta_{s_2,\bar{s}'_1} (\lambda_{i,\underline{s}^2 \rightarrow 1', \underline{p}^2 \rightarrow 1'} \lambda_{i+2\hat{x},\underline{s}'^{1'} \rightarrow 2, \underline{p}'^{1'} \rightarrow 2} - \lambda_{i,\underline{s},\underline{p}} \lambda_{i+2\hat{x},\underline{s}',\underline{p}'}) \quad (\text{B30})$$

$$g_{i,\underline{s},\underline{p}}^{(p,n,34')} = \sum_{\underline{s}',\underline{p}'} \delta_{s_3,\bar{s}'_4} (\lambda_{i,\underline{s}^3 \rightarrow 4', \underline{p}^3 \rightarrow 4'} \lambda_{i+2\hat{x},\underline{s}'^{4'} \rightarrow 3, \underline{p}'^{4'} \rightarrow 3} - \lambda_{i,\underline{s},\underline{p}} \lambda_{i+2\hat{x},\underline{s}',\underline{p}'}) \quad (\text{B31})$$

$$g_{i,\underline{s},\underline{p}}^{(p,n,32')} = \sum_{\underline{s}',\underline{p}'} \delta_{s_3,\bar{s}'_2} (\lambda_{i,\underline{s}^3 \rightarrow 2', \underline{p}^3 \rightarrow 2'} \lambda_{i+2\hat{y},\underline{s}'^{2'} \rightarrow 3, \underline{p}'^{2'} \rightarrow 3} - \lambda_{i,\underline{s},\underline{p}} \lambda_{i+2\hat{y},\underline{s}',\underline{p}'}) \quad (\text{B32})$$

$$g_{i,\underline{s},\underline{p}}^{(p,n,41')} = \sum_{\underline{s}',\underline{p}'} \delta_{s_4,\bar{s}'_1} (\lambda_{i,\underline{s}^4 \rightarrow 1', \underline{p}^4 \rightarrow 1'} \lambda_{i+2\hat{y},\underline{s}'^{1'} \rightarrow 4, \underline{p}'^{1'} \rightarrow 4} - \lambda_{i,\underline{s},\underline{p}} \lambda_{i+2\hat{y},\underline{s}',\underline{p}'}) \quad (\text{B33})$$

$$g_{i,\underline{s},\underline{p}}^{(p,n,43')} = \sum_{\underline{s}',\underline{p}'} \delta_{s_4,\bar{s}'_3} (\lambda_{i,\underline{s}^4 \rightarrow 3', \underline{p}^4 \rightarrow 3'} \lambda_{i-2\hat{x},\underline{s}'^{3'} \rightarrow 4, \underline{p}'^{3'} \rightarrow 4} - \lambda_{i,\underline{s},\underline{p}} \lambda_{i-2\hat{x},\underline{s}',\underline{p}'}) \quad (\text{B34})$$

$$g_{i,\underline{s},\underline{p}}^{(p,n,12')} = \sum_{\underline{s}',\underline{p}'} \delta_{s_1,\bar{s}'_2} (\lambda_{i,\underline{s}^1 \rightarrow 2', \underline{p}^1 \rightarrow 2'} \lambda_{i-2\hat{x},\underline{s}'^{2'} \rightarrow 1, \underline{p}'^{2'} \rightarrow 1} - \lambda_{i,\underline{s},\underline{p}} \lambda_{i-2\hat{x},\underline{s}',\underline{p}'}) \quad (\text{B35})$$

where superscript c in \underline{s}^c or \underline{p}^c suggests the changed index [e.g., $\underline{s}^{1 \rightarrow 4'} = (s'_4, s_2, s_3, s_4)$ and $\underline{s}'^{3' \rightarrow 2} = (s'_1, s'_2, s_2, s'_4)$]. Note that the nonlinearity in Eqs. (B28)-(B35) is derived from the master equation by neglecting the correlation between different clusters.

Similarly, $g_{i,\underline{s},\underline{p}}^{(a,n)}$ represents the contribution from the active exchange across cluster i and neighboring clusters, which is divided into eight terms:

$$g_{i,\underline{s},\underline{p}}^{(a,n)} = g_{i,\underline{s},\underline{p}}^{(a,n,14')} + g_{i,\underline{s},\underline{p}}^{(a,n,23')} + g_{i,\underline{s},\underline{p}}^{(a,n,21')} + g_{i,\underline{s},\underline{p}}^{(a,n,34')} + g_{i,\underline{s},\underline{p}}^{(a,n,32')} + g_{i,\underline{s},\underline{p}}^{(a,n,41')} + g_{i,\underline{s},\underline{p}}^{(a,n,43')} + g_{i,\underline{s},\underline{p}}^{(a,n,12')}. \quad (\text{B36})$$

Specifically,

$$g_{i,\underline{s},\underline{p}}^{(a,n,14')} = \sum_{\underline{s}',\underline{p}'} \delta_{s_1,\bar{s}'_4} [(\varepsilon_{s_1} \delta_{p_1,+ \hat{y}} + \varepsilon_{s'_4} \delta_{p'_4,- \hat{y}}) \lambda_{i,\underline{s}^{1-4'},\underline{p}^{1-4'}} \lambda_{i-2\hat{y},\underline{s}^{4'-1},\underline{p}^{4'-1}} - (\varepsilon_{s_1} \delta_{p_1,- \hat{y}} + \varepsilon_{s'_4} \delta_{p'_4,+ \hat{y}}) \lambda_{i,\underline{s},\underline{p}} \lambda_{i-2\hat{y},\underline{s}',\underline{p}'}] \quad (\text{B37})$$

$$g_{i,\underline{s},\underline{p}}^{(a,n,23')} = \sum_{\underline{s}',\underline{p}'} \delta_{s_2,\bar{s}'_3} [(\varepsilon_{s_2} \delta_{p_2,+ \hat{y}} + \varepsilon_{s'_3} \delta_{p'_3,- \hat{y}}) \lambda_{i,\underline{s}^{2-3'},\underline{p}^{2-3'}} \lambda_{i-2\hat{y},\underline{s}^{3'-2},\underline{p}^{3'-2}} - (\varepsilon_{s_2} \delta_{p_2,- \hat{y}} + \varepsilon_{s'_3} \delta_{p'_3,+ \hat{y}}) \lambda_{i,\underline{s},\underline{p}} \lambda_{i-2\hat{y},\underline{s}',\underline{p}'}] \quad (\text{B38})$$

$$g_{i,\underline{s},\underline{p}}^{(a,n,21')} = \sum_{\underline{s}',\underline{p}'} \delta_{s_2,\bar{s}'_1} [(\varepsilon_{s_2} \delta_{p_2,- \hat{x}} + \varepsilon_{s'_1} \delta_{p'_1,+ \hat{x}}) \lambda_{i,\underline{s}^{2-1'},\underline{p}^{2-1'}} \lambda_{i+2\hat{x},\underline{s}^{1'-2},\underline{p}^{1'-2}} - (\varepsilon_{s_2} \delta_{p_2,+ \hat{x}} + \varepsilon_{s'_1} \delta_{p'_1,- \hat{x}}) \lambda_{i,\underline{s},\underline{p}} \lambda_{i+2\hat{x},\underline{s}',\underline{p}'}] \quad (\text{B39})$$

$$g_{i,\underline{s},\underline{p}}^{(a,n,34')} = \sum_{\underline{s}',\underline{p}'} \delta_{s_3,\bar{s}'_4} [(\varepsilon_{s_3} \delta_{p_3,- \hat{x}} + \varepsilon_{s'_4} \delta_{p'_4,+ \hat{x}}) \lambda_{i,\underline{s}^{3-4'},\underline{p}^{3-4'}} \lambda_{i+2\hat{x},\underline{s}^{4'-3},\underline{p}^{4'-3}} - (\varepsilon_{s_3} \delta_{p_3,+ \hat{x}} + \varepsilon_{s'_4} \delta_{p'_4,- \hat{x}}) \lambda_{i,\underline{s},\underline{p}} \lambda_{i+2\hat{x},\underline{s}',\underline{p}'}] \quad (\text{B40})$$

$$g_{i,\underline{s},\underline{p}}^{(a,n,32')} = \sum_{\underline{s}',\underline{p}'} \delta_{s_3,\bar{s}'_2} [(\varepsilon_{s_3} \delta_{p_3,- \hat{y}} + \varepsilon_{s'_2} \delta_{p'_2,+ \hat{y}}) \lambda_{i,\underline{s}^{3-2'},\underline{p}^{3-2'}} \lambda_{i+2\hat{y},\underline{s}^{2'-3},\underline{p}^{2'-3}} - (\varepsilon_{s_3} \delta_{p_3,+ \hat{y}} + \varepsilon_{s'_2} \delta_{p'_2,- \hat{y}}) \lambda_{i,\underline{s},\underline{p}} \lambda_{i+2\hat{y},\underline{s}',\underline{p}'}] \quad (\text{B41})$$

$$g_{i,\underline{s},\underline{p}}^{(a,n,41')} = \sum_{\underline{s}',\underline{p}'} \delta_{s_4,\bar{s}'_1} [(\varepsilon_{s_4} \delta_{p_4,- \hat{y}} + \varepsilon_{s'_1} \delta_{p'_1,+ \hat{y}}) \lambda_{i,\underline{s}^{4-1'},\underline{p}^{4-1'}} \lambda_{i+2\hat{y},\underline{s}^{1'-4},\underline{p}^{1'-4}} - (\varepsilon_{s_4} \delta_{p_4,+ \hat{y}} + \varepsilon_{s'_1} \delta_{p'_1,- \hat{y}}) \lambda_{i,\underline{s},\underline{p}} \lambda_{i+2\hat{y},\underline{s}',\underline{p}'}] \quad (\text{B42})$$

$$g_{i,\underline{s},\underline{p}}^{(a,n,43')} = \sum_{\underline{s}',\underline{p}'} \delta_{s_4,\bar{s}'_3} [(\varepsilon_{s_4} \delta_{p_4,+ \hat{x}} + \varepsilon_{s'_3} \delta_{p'_3,- \hat{x}}) \lambda_{i,\underline{s}^{4-3'},\underline{p}^{4-3'}} \lambda_{i-2\hat{x},\underline{s}^{3'-4},\underline{p}^{3'-4}} - (\varepsilon_{s_4} \delta_{p_4,- \hat{x}} + \varepsilon_{s'_3} \delta_{p'_3,+ \hat{x}}) \lambda_{i,\underline{s},\underline{p}} \lambda_{i-2\hat{x},\underline{s}',\underline{p}'}] \quad (\text{B43})$$

$$g_{i,\underline{s},\underline{p}}^{(a,n,12')} = \sum_{\underline{s}',\underline{p}'} \delta_{s_1,\bar{s}'_2} [(\varepsilon_{s_1} \delta_{p_1,+ \hat{x}} + \varepsilon_{s'_2} \delta_{p'_2,- \hat{x}}) \lambda_{i,\underline{s}^{1-2'},\underline{p}^{1-2'}} \lambda_{i-2\hat{x},\underline{s}^{2'-1},\underline{p}^{2'-1}} - (\varepsilon_{s_1} \delta_{p_1,- \hat{x}} + \varepsilon_{s'_2} \delta_{p'_2,+ \hat{x}}) \lambda_{i,\underline{s},\underline{p}} \lambda_{i-2\hat{x},\underline{s}',\underline{p}'}]. \quad (\text{B44})$$

Note that the nonlinearity in Eqs. (B37)-(B44) is derived from the master equation by neglecting the correlation between different clusters in a similar way as Eqs. (B28)-(B35).

Lastly, $g_{i,\underline{s},\underline{p}}^{(r)}$ represents the rotation of polarity within cluster i :

$$g_{i,\underline{s},\underline{p}}^{(r)} = \sum_{n=1}^4 \gamma(\lambda_{i,\underline{s},\underline{p}^{n:R}} + \lambda_{i,\underline{s},\underline{p}^{n:R^{-1}}} - 2\lambda_{i,\underline{s},\underline{p}}). \quad (\text{B45})$$

Here, superscript r in \underline{p}^r suggests the index and direction for rotated polarity [e.g., $\underline{p}^{2:R} = (p_1, R p_2, p_3, p_4)$ and $\underline{p}^{3:R^{-1}} = (p_1, p_2, R^{-1} p_3, p_4)$], where R and R^{-1} represent counterclockwise and clockwise rotations by 90° , respectively [e.g., $R(+\hat{y}) = -\hat{x}$].

-
- | | |
|---|--|
| <p>[1] S. Ramaswamy, R. Aditi Simha, and J. Toner, Active nematics on a substrate: Giant number fluctuations and long-time tails, <i>EPL</i> 62, 196 (2003).</p> <p>[2] S. Shankar, S. Ramaswamy, and M. C. Marchetti, Low-noise phase of a two-dimensional active nematic system, <i>Phys. Rev. E</i> 97, 012707 (2018).</p> <p>[3] J. Dunkel, S. Heidenreich, K. Drescher, H. H. Wensink, M. Bär, and R. E. Goldstein, Fluid dynamics of bacterial turbulence, <i>Phys. Rev. Lett.</i> 110, 228102 (2013).</p> <p>[4] M. C. Marchetti, J. F. Joanny, S. Ramaswamy, T. B. Liverpool, J. Prost, M. Rao, and R. A. Simha, Hydrodynamics of soft active matter, <i>Rev. Mod. Phys.</i> 85, 1143 (2013).</p> <p>[5] G. Gompper, H. A. Stone, C. Kurzthaler, D. Saintillan, F. Peruani, D. A. Fedosov, T. Auth, C. Cottin-Bizonne, C. Ybert, E. Clément, T. Darnige, A. Lindner, R. E. Goldstein, B. Liebchen, J. Binysh, A. Souslov, L. Isa, R. di Leonardo, G. Frangipane, H. Gu, B. J. Nelson, F. Brauns, M. C. Marchetti, F. Cichos, V.-L. Heuthe, C. Bechinger, A. Korman, O. Feinerman, A. Cavagna, I. Giardina, H. Jeckel, and K. Drescher, The 2025 motile active matter roadmap, <i>J. Phys. Condens. Matter</i> 37, 143501 (2025).</p> | <p>[6] M. Te Vrugt and R. Wittkowski, Metareview: a survey of active matter reviews, <i>Eur. Phys. J. E</i> 48, 12 (2025).</p> <p>[7] B. Szabó, G. J. Szöllösi, B. Gönci, Z. Jurányi, D. Selmeczi, and T. Vicsek, Phase transition in the collective migration of tissue cells: experiment and model, <i>Phys. Rev. E</i> 74, 061908 (2006).</p> <p>[8] D. Nishiguchi, K. H. Nagai, H. Chaté, and M. Sano, Long-range nematic order and anomalous fluctuations in suspensions of swimming filamentous bacteria, <i>Phys. Rev. E</i> 95, 020601 (2017).</p> <p>[9] K. Kawaguchi, R. Kageyama, and M. Sano, Topological defects control collective dynamics in neural progenitor cell cultures, <i>Nature</i> 545, 327 (2017).</p> <p>[10] G. Liu, A. Patch, F. Bahar, D. Yllanes, R. D. Welch, M. C. Marchetti, S. Thutupalli, and J. W. Shaevitz, Self-Driven Phase Transitions Drive <i>Myxococcus xanthus</i> Fruiting Body Formation, <i>Phys. Rev. Lett.</i> 122, 248102 (2019).</p> <p>[11] T. H. Tan, A. Mietke, J. Li, Y. Chen, H. Higinbotham, P. J. Foster, S. Gokhale, J. Dunkel, and N. Fakhri, Odd dynamics of living chiral crystals, <i>Nature</i> 607, 287 (2022).</p> <p>[12] J. Deseigne, O. Dauchot, and H. Chaté, Collective motion of vibrated polar disks, <i>Phys. Rev. Lett.</i> 105, 098001 (2010).</p> |
|---|--|

- [13] J. Palacci, S. Sacanna, A. P. Steinberg, D. J. Pine, and P. M. Chaikin, Living crystals of light-activated colloidal surfers, *Science* **339**, 936 (2013).
- [14] A. Bricard, J.-B. Caussin, N. Desreumaux, O. Dauchot, and D. Bartolo, Emergence of macroscopic directed motion in populations of motile colloids, *Nature* **503**, 95 (2013).
- [15] I. Buttinoni, J. Bialké, F. Kümmel, H. Löwen, C. Bechinger, and T. Speck, Dynamical clustering and phase separation in suspensions of self-propelled colloidal particles, *Phys. Rev. Lett.* **110**, 238301 (2013).
- [16] N. Kumar, H. Soni, S. Ramaswamy, and A. K. Sood, Flocking at a distance in active granular matter, *Nat. Commun.* **5**, 4688 (2014).
- [17] F. Ginot, I. Theurkauff, F. Detcheverry, C. Ybert, and C. Cottin-Bizonne, Aggregation-fragmentation and individual dynamics of active clusters, *Nat. Commun.* **9**, 696 (2018).
- [18] A. Deblais, T. Barois, T. Guerin, P. H. Delville, R. Vaudaine, J. S. Lintuvuori, J. F. Boudet, J. C. Baret, and H. Kellay, Boundaries Control Collective Dynamics of Inertial Self-Propelled Robots, *Phys. Rev. Lett.* **120**, 188002 (2018).
- [19] D. Geyer, D. Martin, J. Tailleur, and D. Bartolo, Freezing a Flock: Motility-Induced Phase Separation in Polar Active Liquids, *Phys. Rev. X* **9**, 031043 (2019).
- [20] A. Chardac, S. Shankar, M. C. Marchetti, and D. Bartolo, Emergence of dynamic vortex glasses in disordered polar active fluids, *Proc. Natl. Acad. Sci. U.S.A.* **118**, e2018218118 (2021).
- [21] G. Wang, T. V. Phan, S. Li, M. Wombacher, J. Qu, Y. Peng, G. Chen, D. I. Goldman, S. A. Levin, R. H. Austin, and L. Liu, Emergent Field-Driven Robot Swarm States, *Phys. Rev. Lett.* **126**, 108002 (2021).
- [22] T. Vicsek, A. Czirók, E. Ben-Jacob, I. Cohen, I. and O. Shochet, Novel type of phase transition in a system of self-driven particles, *Phys. Rev. Lett.* **75**, 1226 (1995).
- [23] J. Toner and Y. Tu, Long-Range Order in a Two-Dimensional Dynamical XY Model: How Birds Fly Together, *Phys. Rev. Lett.* **75**, 4326 (1995).
- [24] D. Needleman and Z. Dogic, Active matter at the interface between materials science and cell biology, *Nat. Rev. Mater.* **2**, 1 (2017).
- [25] H. Chaté, Dry Aligning Dilute Active Matter, *Annu. Rev. Condens. Matter Phys.* **11**, 189 (2020).
- [26] J. Toner and Y. Tu, Flocks, herds, and schools: A quantitative theory of flocking, *Phys. Rev. E* **58**, 4828 (1998).
- [27] J. Toner, Reanalysis of the hydrodynamic theory of fluid, polar-ordered flocks, *Phys. Rev. E* **86**, 031918 (2012).
- [28] J. Toner, Birth, death, and flight: a theory of Malthusian flocks, *Phys. Rev. Lett.* **108**, 088102 (2012).
- [29] B. Mahault, F. Ginelli, and H. Chaté, Quantitative Assessment of the Toner and Tu Theory of Polar Flocks, *Phys. Rev. Lett.* **123**, 218001 (2019).
- [30] J. Codina, B. Mahault, H. Chaté, J. Dobnikar, I. Pagonabarraga, and X.-Q. Shi, Small Obstacle in a Large Polar Flock, *Phys. Rev. Lett.* **128**, 218001 (2022).
- [31] M. Besse, H. Chaté, and A. Solon, Metastability of Constant-Density Flocks, *Phys. Rev. Lett.* **129**, 268003 (2022).
- [32] B. Benvegnen, O. Granek, S. Ro, R. Yaacoby, H. Chaté, Y. Kafri, D. Mukamel, A. Solon, and J. Tailleur, Metastability of Discrete-Symmetry Flocks, *Phys. Rev. Lett.* **131**, 218301 (2023).
- [33] M. E. Cates and C. Nardini, Active phase separation: new phenomenology from non-equilibrium physics, arXiv:2412.02854.
- [34] M. E. Cates and J. Tailleur, Motility-Induced Phase Separation, *Annu. Rev. Condens. Matter Phys.* **6**, 219 (2015).
- [35] Y. Fily and M. C. Marchetti, Athermal phase separation of self-propelled particles with no alignment, *Phys. Rev. Lett.* **108**, 235702 (2012).
- [36] D. Martin, J. O’Byrne, M. E. Cates, E. Fodor, C. Nardini, J. Tailleur, and F. van Wijland, Statistical mechanics of active Ornstein-Uhlenbeck particles, *Phys. Rev. E* **103**, 032607 (2021).
- [37] A. G. Thompson, J. Tailleur, M. E. Cates, and R. A. Blythe, Lattice models of nonequilibrium bacterial dynamics, *J. Stat. Mech.* **2011**, P02029 (2011).
- [38] R. Wittkowski, A. Tiribocchi, J. Stenhammar, R. J. Allen, D. Marenduzzo, and M. E. Cates, Scalar ϕ^4 field theory for active-particle phase separation, *Nat. Commun.* **5**, 4351 (2014).
- [39] E. Tjhung, C. Nardini, and M. E. Cates, Cluster Phases and Bubbly Phase Separation in Active Fluids: Reversal of the Ostwald Process, *Phys. Rev. X* **8**, 031080 (2018).
- [40] L. Caprini, U. Marini Bettolo Marconi, and A. Puglisi, Spontaneous Velocity Alignment in Motility-Induced Phase Separation, *Phys. Rev. Lett.* **124**, 078001 (2020).
- [41] J. Tailleur and M. E. Cates, Statistical mechanics of interacting run-and-tumble bacteria, *Phys. Rev. Lett.* **100**, 218103 (2008).
- [42] A. P. Solon, J. Stenhammar, M. E. Cates, Y. Kafri, and J. Tailleur, Generalized thermodynamics of phase equilibria in scalar active matter, *Phys. Rev. E* **97**, 020602 (2018).
- [43] A. P. Solon, J. Stenhammar, M. E. Cates, Y. Kafri, and J. Tailleur, Generalized thermodynamics of motility-induced phase separation: phase equilibria, Laplace pressure, and change of ensembles, *New J. Phys.* **20**, 075001 (2018).
- [44] F. Caballero, C. Nardini, and M. E. Cates, From bulk to microphase separation in scalar active matter: a perturbative renormalization group analysis, *J. Stat. Mech.* **2018**, 123208 (2018).
- [45] R. Singh and M. E. Cates, Hydrodynamically Interrupted Droplet Growth in Scalar Active Matter, *Phys. Rev. Lett.* **123**, 148005 (2019).
- [46] X.-Q. Shi, G. Fausti, H. Chaté, C. Nardini, and A. Solon, Self-Organized Critical Coexistence Phase in Repulsive Active Particles, *Phys. Rev. Lett.* **125**, 168001 (2020).
- [47] C. B. Caporusso, P. Digregorio, D. Levis, L. F. Cugliandolo, and G. Gonnella, Motility-Induced Microphase and Macrophase Separation in a Two-Dimensional Active Brownian Particle System, *Phys. Rev. Lett.* **125**, 178004 (2020).
- [48] H. Nakano and K. Adachi, Universal properties of repulsive self-propelled particles and attractive driven particles, *Phys. Rev. Res.* **6**, 013074 (2024).
- [49] G. Fausti, M. E. Cates, and C. Nardini, Statistical properties of microphase and bubbly phase-separated active fluids, *Phys. Rev. E* **110**, L042103 (2024).
- [50] M. Rubinstein and R. H. Colby, *Polymer Physics* (Oxford University Press, 2003).
- [51] T. Speck, Critical behavior of active Brownian particles: Connection to field theories, *Phys. Rev. E* **105**, 064601 (2022).
- [52] B. Partridge and C. F. Lee, Critical Motility-Induced Phase Separation Belongs to the Ising Universality Class, *Phys. Rev. Lett.* **123**, 068002 (2019).
- [53] C. Maggi, M. Paoluzzi, A. Crisanti, E. Zaccarelli, and N. Gnan, Universality class of the motility-induced critical point in large scale off-lattice simulations of active particles, *Soft Matter* **17**, 3807 (2021).
- [54] N. Gnan and C. Maggi, Critical behavior of quorum-sensing active particles, *Soft Matter* **18**, 7654 (2022).
- [55] F. Jiechao and K. O. Ahmad, Critical motility-induced phase separation in three dimensions is consistent with Ising universality, arXiv:2502.09069.
- [56] J. T. Siebert, F. Dittrich, F. Schmid, K. Binder, T. Speck, and

- P. Virnau, Critical behavior of active Brownian particles, *Phys. Rev. E* **98**, 030601 (2018).
- [57] F. Dittrich, T. Speck, and P. Virnau, Critical behavior in active lattice models of motility-induced phase separation, *Eur. Phys. J. E* **44**, 53 (2021).
- [58] L. P. Kadanoff, W. Götze, D. Hamblen, R. Hecht, E. A. S. Lewis, V. V. Palciauskas, M. Rayl, J. Swift, D. Aspnes, and J. Kane, Static Phenomena Near Critical Points: Theory and Experiment, *Rev. Mod. Phys.* **39**, 395 (1967).
- [59] R. Zakine, J. Garnier-Brun, A.-C. Becharat, and M. Benzaquen, Socioeconomic agents as active matter in nonequilibrium Sakoda-Schelling models, *Phys. Rev. E* **109**, 044310 (2024).
- [60] R. Soto and R. Golestanian, Run-and-tumble dynamics in a crowded environment: persistent exclusion process for swimmers, *Phys. Rev. E* **89**, 012706 (2014).
- [61] S. Whitelam, K. Klymko, and D. Mandal, Phase separation and large deviations of lattice active matter, *J. Chem. Phys.* **148**, 154902 (2018).
- [62] M. Kourbane-Houssene, C. Erignoux, T. Bodineau, and J. Tailleur, Exact Hydrodynamic Description of Active Lattice Gases, *Phys. Rev. Lett.* **120**, 268003 (2018).
- [63] A. P. Solon and J. Tailleur, Revisiting the flocking transition using active spins, *Phys. Rev. Lett.* **111**, 078101 (2013).
- [64] A. P. Solon and J. Tailleur, Flocking with discrete symmetry: The two-dimensional active Ising model, *Phys. Rev. E* **92**, 042119 (2015).
- [65] A. I. Curatolo, M. R. Evans, Y. Kafri, and J. Tailleur, Multilane driven diffusive systems, *J. Phys. A* **49**, 095601 (2016).
- [66] S. Hermann, P. Krinninger, D. de Las Heras, and M. Schmidt, Phase coexistence of active Brownian particles, *Phys. Rev. E* **100**, 052604 (2019).
- [67] S. Hermann and M. Schmidt, Active interface polarization as a state function, *Phys. Rev. Research* **2**, 022003 (2020).
- [68] A. K. Omar, H. Row, S. A. Mallory, and J. F. Brady, Mechanical theory of nonequilibrium coexistence and motility-induced phase separation, *Proc. Natl. Acad. Sci. U.S.A.* **120**, e2219900120 (2023).
- [69] P. Virtanen, R. Gommers, T. E. Oliphant, M. Haberland, T. Reddy, D. Cournapeau, E. Burovski, P. Peterson, W. Weckesser, J. Bright, S. J. van der Walt, M. Brett, J. Wilson, K. J. Millman, N. Mayorov, A. R. J. Nelson, E. Jones, R. Kern, E. Larson, C. J. Carey, Í. Polat, Y. Feng, E. W. Moore, J. VanderPlas, D. Laxalde, J. Perktold, R. Cimrman, I. Henriksen, E. A. Quintero, C. R. Harris, A. M. Archibald, A. H. Ribeiro, F. Pedregosa, P. van Mulbregt, and SciPy 1.0 Contributors, SciPy 1.0: fundamental algorithms for scientific computing in Python, *Nat. Methods* **17**, 261 (2020).
- [70] P. M. Chaikin and T. C. Lubensky, *Principles of Condensed Matter Physics* (Cambridge University Press, 1995).
- [71] T. Speck, J. Bialké, A. M. Menzel, and H. Löwen, Effective Cahn-Hilliard Equation for the Phase Separation of Active Brownian Particles, *Phys. Rev. Lett.* **112**, 218304 (2014).
- [72] T. Speck, A. M. Menzel, J. Bialké, and H. Löwen, Dynamical mean-field theory and weakly non-linear analysis for the phase separation of active Brownian particles, *J. Chem. Phys.* **142**, 224109 (2015).
- [73] P. C. Hohenberg and B. I. Halperin, Theory of dynamic critical phenomena, *Rev. Mod. Phys.* **49**, 435 (1977).
- [74] K. Leung, Finite-size scaling of driven diffusive systems: Theory and Monte Carlo studies, *Phys. Rev. Lett.* **66**, 453 (1991).
- [75] J.-S. Wang, Anisotropic finite-size scaling analysis of a two-dimensional driven diffusive system, *J. Stat. Phys.* **82**, 1409 (1996).
- [76] K. Adachi, K. Takasan, and K. Kawaguchi, Activity-induced phase transition in a quantum many-body system, *Phys. Rev. Res.* **4**, 013194 (2022).
- [77] D. Landau and K. Binder, *A Guide to Monte Carlo Simulations in Statistical Physics* (Cambridge University Press, 2021).
- [78] K. Harada, Kernel method for corrections to scaling, *Phys. Rev. E* **92**, 012106 (2015).
- [79] T. Kolb and D. Klotsa, Active binary mixtures of fast and slow hard spheres, *Soft Matter* **16**, 1967 (2020).
- [80] A. P. Solon, H. Chaté, and J. Tailleur, From phase to microphase separation in flocking models: the essential role of nonequilibrium fluctuations, *Phys. Rev. Lett.* **114**, 068101 (2015).
- [81] S. Ngo, A. Peshkov, I. S. Aranson, E. Bertin, F. Ginelli, and H. Chaté, Large-scale chaos and fluctuations in active nematics, *Phys. Rev. Lett.* **113**, 038302 (2014).
- [82] <https://github.com/adachi24/active-binary-mixture>.
- [83] L. Onsager, Crystal Statistics. I. A Two-Dimensional Model with an Order-Disorder Transition, *Phys. Rev.* **65**, 117 (1944).
- [84] P. Tamayo and W. Klein, Critical dynamics and global conservation laws, *Phys. Rev. Lett.* **63**, 2757 (1989).
- [85] A. J. Bray, Comment on “Critical dynamics and global conservation laws”, *Phys. Rev. Lett.* **66**, 2048 (1991).
- [86] P. Tamayo and W. Klein, Tamayo and Klein reply, *Phys. Rev. Lett.* **66**, 2049 (1991).
- [87] L. L. Moseley, P. W. Gibbs, and N. Jan, Kawasaki dynamics with infinite-range spin exchange, *J. Stat. Phys.* **67**, 813 (1992).